ADVANCED ENERGY MATERIALS
www.advenergymat.de

Investigations toward a Non-Aqueous Hybrid Redox-Flow Battery with a Manganese-Based Anolyte and Catholyte

*Maximilian Schmucker, Tyler A. Gully, Alexei Schmidt, Benjamin Schmidt, Kolja Bromberger, Joey Disch, Burkhard Butschke, Benedikt Burgenmeister, Karsten Sonnenberg, Sebastian Riedel, and Ingo Krossing**

A new all-Manganese flow battery (all-MFB) as a non-aqueous hybrid redox-flow battery is reported. The discharged active material $[Cat]_2[Mn^{II}Cl_4]$ (Cat = organic cation) utilized in both half-cells supports a long cycle life. The reversible oxidation of $[Mn^{II}Cl_4]^{2-}$ to $[Mn^{III}Cl_5]^{2-}$ at the positive electrode and manganese metal deposition from $[Mn^{II}Cl_4]^{2-}$ at the negative electrode give a cell voltage of 2.59 V. Suitable electrolytes are prepared and optimized, followed by a characterization in static battery cells and in a pumped flow-cell. Several electrode materials, solvents, and membranes are tested for their feasibility in the all-MFB. An electrolyte consisting of $[EMP]_2[MnCl_4]$ and some solvent γ-butyrolactone is cycled 500 times, both in a static as well as a flow-cell, over a period of two months, with coulombic efficiencies up to 83%. With the electrolytes prepared in this work, energy densities up to 74 Wh L^{-1} are possible, exceeding the VRFB benchmark system, using solely the cheap and abundant element manganese as the active material. Although further optimizations are necessary, this system represents a new and promising setup toward sustainable stationary energy storage.

1. Introduction

The importance of electrical energy-storage systems (EES), for a successful integration of intermittent renewable energy sources into the electrical grid is beyond dispute.[1–4] For mobile applications, lithium ion batteries (LIBs) with high energy density prevail.[2,5,6] Although many efforts focus on alternative chemical systems (e.g., multivalent Al, Mg, and Ca), it is hard to imagine that LIBs will disappear in the near future.[4,7] Yet, for large scale stationary EES, there is no such prevailing technology. Although other alternatives, like pumped hydro or fuel cells are available, batteries are amongst the most promising technologies for this purpose.[1,3,8] With the energy density being slightly less relevant, other redox active materials could be employed in large scale EES, i.e., redox-flow batteries (RFBs) with their very long cycle life and decoupled capacity, power and energy output.[2,9,10] Their benchmark is the all-vanadium redox-flow battery (VRFB) with V^{II}/V^{III} and V^{IV}/V^{V} redox couples,[2] as well as a 15 000–20 000 charge/discharge cycles lifetime and an acceptable energy density of 25–35 Wh L^{-1} installed in up to 60 MWh capacity EES.[2,6] However, probably due to the high cost, a commercial breakthrough still has to come.[2,6,9] Considering abundancy and cost, few elements are suitable as redox active material in sustainable batteries.[4,11] Manganese is one of them and, therefore, finds application in LIB-cathode active materials (e.g., $LiMn_2O_4$ or $Li[Ni_{0.8}Co_{0.1}Mn_{0.1}]O_2$) or in cathode materials of primary batteries (MnO_2).[5,12] However, to the best of our knowledge, only one battery system exclusively using manganese compounds at both electrodes is described,[13] i.e., $Mn(acac)_3$ acetonitrile (MeCN) solutions with the Mn^{II}/Mn^{III} couple at the negative and the Mn^{III}/Mn^{IV} couple at the positive electrode. Yet, with E_{cell} of 1.1 V the system does not exploit the large potential range advantage of a non-aqueous electrolyte. Already the aqueous standard potential difference ΔE^0 of Mn^0/Mn^{II} and Mn^{II}/Mn^{III} redox couples amounts to an impressive 2.69 V. In addition, the Mn volumetric specific capacity is 7034.7 Ah L^{-1} (two-electron-process). It clearly exceeds that of zinc (5853.8 Ah L^{-1}), which in the zinc

M. Schmucker, A. Schmidt, Dr. B. Butschke, Dr. B. Burgenmeister, Prof. I. Krossing
Institut für Anorganische und Analytische Chemie and Freiburger Materialforschungszentrum (FMF)
Albert-Ludwigs-Universität Freiburg
Albertstr. 21, 79104 Freiburg, Germany
E-mail: krossing@uni-freiburg.de

T. A. Gully, Dr. B. Schmidt, Dr. K. Sonnenberg, Prof. S. Riedel
Fachbereich Biologie
Chemie
Pharmazie
Institut für Chemie und Biochemie – Anorganische Chemie
Freie Universität Berlin
Fabeckstr. 34–36, 14195 Berlin, Germany

K. Bromberger, J. Disch
Bereich Wasserstofftechnologien
Fraunhofer-Institut für Solare Energiesysteme ISE
Heidenhofstr. 2, 79110 Freiburg, Germany

The ORCID identification number(s) for the author(s) of this article can be found under https://doi.org/10.1002/aenm.202101261.

© 2021 The Authors. Advanced Energy Materials published by Wiley-VCH GmbH. This is an open access article under the terms of the Creative Commons Attribution-NonCommercial License, which permits use, distribution and reproduction in any medium, provided the original work is properly cited and is not used for commercial purposes.

DOI: 10.1002/aenm.202101261

bromine flow battery (ZBFB) represents the benchmark system for hybrid redox-flow batteries.[2] Therefore, the two-electron-deposition and stripping of Mn as possible negative electrode reactions may lead to an all-MFB with favorable energy density. Since hydrogen evolution is one of the major side reactions upon manganese deposition (E^0 = −1.18 V) and oxygen evolution may compete with the Mn^{II}/Mn^{III} redox couple (E^0 = +1.51 V), non-aqueous electrolytes are preferable.[14] To increase cycle-life, the same electrochemically active species has to be used in both half-cells. Therefore, a manganese ion allowing manganese deposition, but also forming stable Mn^{III}/Mn^{IV} compounds was needed. Chloromanganates were identified as an option for the active species. Of those, the Cambridge Structural Database includes 49 entries for the $[Mn^{II}Cl_4]^{2-}$ anion, but only three containing $[Mn^{III}Cl_5]^{2-}$.[15] Only three inorganic variants are known for the $[Mn^{IV}Cl_6]^{2-}$ anion (Inorganic Crystal Structure Database).[16–18] However, well characterized $[Mn^{III}Cl_5]^{2-}$ and $[Mn^{IV}Cl_6]^{2-}$ salts are known (vide infra = v.i.). Thus, starting from well-known $[Mn^{II}Cl_4]^{2-}$,[19–27] Equations (1) and (2) represent possible cell reactions of an all-Mn battery:

$$3[Mn^{II}Cl_4]^{2-} \underset{\text{charge}}{\overset{\text{discharge}}{\rightleftharpoons}} Mn^0 + 2[Mn^{III}Cl_5]^{2-} + 2Cl^- \quad (1)$$

$$2[Mn^{II}Cl_4]^{2-} \underset{\text{charge}}{\overset{\text{discharge}}{\rightleftharpoons}} Mn^0 + [Mn^{IV}Cl_6]^{2-} + 2Cl^- \quad (2)$$

At the positive electrode an oxidation of $[Mn^{II}Cl_4]^{2-}$ into known $[Mn^{III}Cl_5]^{2-}$ or $[Mn^{IV}Cl_6]^{2-}$ is conceivable.[16,17,28–34] Reaching the oxidation state +IV in a two-electron-process in $[Mn^{IV}Cl_6]^{2-}$ would favorably improve the energy density. Yet, the expected high redox potential of Mn^{IV} might lead to the formation of Cl_2 as main or side reaction. In addition, non-aqueous manganese deposition from $[Mn^{II}Cl_4]^{2-}$ is unknown.[35,36] Table S19 (Supporting Information) includes the expected energy densities for an all-Mn battery based on the conservative Equation (1) with 1–2 mol L^{-1} electrolyte concentration and a cell potential E_{cell} of 2.69 V (aqueous redox potentials). With a theoretical energy density around 44–87 Wh Kg^{-1}, the all-Mn battery would have the potential to exceed VRFB and ZBFB in energy density and use the cheap and abundant elements manganese and chlorine. Here we investigated, if such a battery can be realized.

2. Results and Discussion

This paper is organized by a synthesis and characterization section that demonstrates the feasibility of the proposed battery chemistry on classical chemical and electrochemical grounds before investigating the battery performance in static symmetric, half as well as full cells, and finally in pumped flow cells. A section on the performance of the all-MFB discussing all experimental data is placed at the end, after describing the flow operation.

2.1. Synthesis and Characterization of the $[Cat]_2[Mn^{II}Cl_4]$ Salts

$[Cat]_2[Mn^{II}Cl_4]$-syntheses with organic cations $[Cat]^+$ are reported since 1959[27] and available according to Equation (3) in yields >99%; we found the products to be stable under atmospheric conditions. Focus is placed on the $[Mn^{II}Cl_4]^{2-}$ salts with 1-butyl-1-methylpyrrolidinium ($[BMP]^+$) and 1-ethyl-1-methylpyrrolidinium ($[EMP]^+$) cation; other cations were tested (Supporting Information).

$$MnCl_2 + 2[Cat]Cl \xrightarrow[\text{e.g. MeCN}]{\text{organic solvent}} [Cat]_2[MnCl_4] \quad (3)$$

All syntheses were performed under inert conditions to prevent contamination with water and its electrochemical side reactions. The organic cation $[Cat]^+$ in the product can easily be varied by simply using the chloride salt [Cat]Cl of the desired cation, also salts with two different cations are possible ($[Cat_1][Cat_2][Mn^{II}Cl_4]$). This gives access to a broad variety of different $[Mn^{II}Cl_4]^{2-}$ salts with electrochemically inert cations that could be used to influence the morphology of the electrochemical metal deposition,[37] optimize solubility, conductivity, and viscosity of the electrolyte. $[Mn^{II}Cl_4]^{2-}$ salts have prior been extensively characterized by scXRD, UV/Vis-, IR-, and Raman spectroscopy.[19–26,38,39] **Figure 1**a,b shows the IR- and the Raman spectra of solid $[BMP]_2[Mn^{II}Cl_4]$ relevant to this work and Table S1 (Supporting Information) contains the corresponding stretching frequencies that agree with the literature.

Raman- and UV/Vis spectroscopy demonstrate that $[Mn^{II}Cl_4]^{2-}$ is not stable in the presence of water (see Figure S3, Supporting Information), since the ν_1-stretching frequency disappeared completely. In contrast, in MeCN- and GBL-solutions the relevant ν_1-stretching frequencies were observed (see Figure 1), showing that the $[Mn^{II}Cl_4]^{2-}$-anion is stable and the respective solvents are suitable for electrolyte preparation. This is further supported by the UV/Vis spectra (Figure 1c,d and Table S2: Supporting Information).

2.2. Electrochemical Investigations toward Battery Application

2.2.1. Spectroelectrochemistry

The charged active species in the all-MFB – the $[Mn^{III}Cl_5]^{2-}$ anion – was prior characterized with scXRD, UV/Vis- Raman- and IR-spectroscopy,[28–32,40] but all known preparation routes start with Mn^{III}- or Mn^{IV}-species. By contrast, in the all-MFB the $[Mn^{II}Cl_4]^{2-}$ is electrochemically oxidized to $[Mn^{III}Cl_5]^{2-}$. **Figure 2**a shows the CV of $EL_{GBL\text{-}BMP\text{-}50}$. The current response is assigned to a reversible oxidation of $[Mn^{II}Cl_4]^{2-}$ with a half-peak potential ($E_{p/2}$) at 1.17 V versus Fc/Fc^+ using a platinum working electrode (Pt-WE) and 1.28 V versus Fc/Fc^+ using a glassy carbon working electrode (GC-WE). These potentials are rather close to the Mn^{2+}/Mn^{3+} redox couple in aqueous media (1.11 V vs Fc/Fc^+).[41,42] The characteristic dark green coloration (see Figure 2b) suggested $[Mn^{III}Cl_5]^{2-}$ formation at the WE during the anodic scan.

Spectroelectrochemical Raman and UV/Vis-measurements, which easily distinguish $[Mn^{II}Cl_4]^{2-}$ and $[Mn^{III}Cl_5]^{2-}$, were conducted. In Figure 2c) the Raman spectra of tetrahedral $[Mn^{II}Cl_4]^{2-}$ as $[EMP]_2[Mn^{II}Cl_4]$ and $[BMP]_2[Mn^{II}Cl_4]$ display the characteristic ν_1-stretching frequency of the anion at 251 and 253 cm^{-1}, respectively. After applying a potential

© 2021 The Authors. Advanced Energy Materials published by Wiley-VCH GmbH

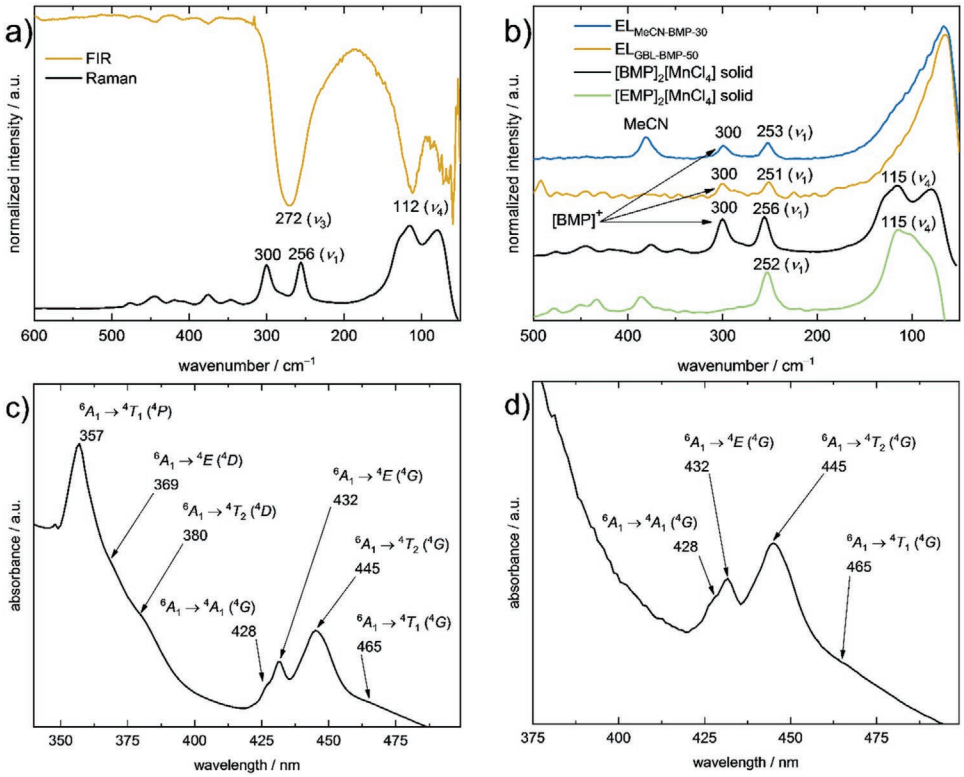

Figure 1. a) IR- and Raman spectra of solid $[BMP]_2[Mn^{II}Cl_4]$. b) Raman spectra of $[BMP]_2[Mn^{II}Cl_4]$ and $[EMP]_2[Mn^{II}Cl_4]$ as solids and $[BMP]_2[Mn^{II}Cl_4]$ dissolved in GBL (50 wt% GBL, $c = 1.2$ mol L^{-1}, $EL_{GBL\text{-}BMP\text{-}50}$) and MeCN (30 wt% MeCN, $c = 1.6$ mol L^{-1}, $EL_{MeCN\text{-}BMP\text{-}30}$). The stretching mode at 300 cm^{-1} can be assigned to $[BMP]^+$, since it is not observed in the spectrum of $[EMP]_2[Mn^{II}Cl_4]$. c) UV/Vis spectrum of $[BMP]_2[Mn^{II}Cl_4]$ in MeCN (90 wt% MeCN, $c = 3.2$ mmol L^{-1}). d) UV/Vis spectrum of $[BMP]_2[Mn^{II}Cl_4]$ in GBL (90 wt% GBL, $c = 0.22$ mol L^{-1}).

of 1.65 V versus q-Pt, a new band at 289 cm^{-1} appears. For the $[BMP]^+$ cation, a band at 300 cm^{-1} (cf. Figure 1b) slightly obscures this region, but it can be clearly observed in the spectrum starting from $[EMP]_2[Mn^{II}Cl_4]$. Comparison with known C_{4v}-symmetric $[Mn^{III}Cl_5]^{2-}$ compounds in Table S7 (Supporting Information) reveals strongest vibrational bands between 289 and 296 cm^{-1}, suggesting that $[Mn^{III}Cl_5]^{2-}$ can be formed electrochemically from $[Mn^{II}Cl_4]^{2-}$. Also, the Raman spectra of the chemically with dichlorine oxidized $[BMP]_2[Mn^{II}Cl_4]$ and $[NEt_4]_2[Mn^{II}Cl_4]$ include the characteristic $[Mn^{III}Cl_5]^{2-}$ stretch at 292 and 287 cm^{-1} (Figure S7, Supporting Information). As a final proof that $[Mn^{III}Cl_5]^{2-}$ forms electrochemically, a crystal structure was obtained from the electrochemical oxidation product of $[NEt_4]_2[Mn^{II}Cl_4]$ (see Figure 2). Since the electrooxidation of $[NEt_4]_2[Mn^{II}Cl_4]$ in MeCN was not quantitative, a cocrystal with $[Mn^{II}Cl_4]^{2-}$ was formed. In all of these experiments the dark green coloration of $[Mn^{III}Cl_5]^{2-}$ was characteristic and UV/Vis-spectroscopy further supports the electrochemical formation of $[Mn^{III}Cl_5]^{2-}$. In Figure 2d) the electronic transitions of $[Mn^{II}Cl_4]^{2-}$ at 431 and 446 nm are visible when no voltage is applied. After applying 1.74 V versus q-Pt or more, these transitions vanish and the intense transitions of $[Mn^{III}Cl_5]^{2-}$ become visible. Table S8 (Supporting Information) shows the assignments of the respective transitions, in accordance with the literature. The spectroelectrochemical analysis in MeCN with Raman and UV/Vis spectra is shown in Figure S6 (Supporting Information).

2.2.2. Mn Electrodeposition from $[Mn^{II}Cl_4]^{2-}$ Solutions

Manganese can be deposited from aqueous solutions[14] and, although hydrogen evolution is a major side reaction, only few reports on manganese-deposition from non-aqueous media are known.[35,36] Yet, depositions from non-aqueous $[Mn^{II}Cl_4]^{2-}$ solution are unknown but possible from the related, but water containing, deep eutectic solvent choline chloride + urea (1:2) upon addition of $Mn^{II}Cl_2 \cdot 4H_2O$.[43] To investigate, whether electrochemical deposition and striping of manganese from an anhydrous solution is possible, the CVs of three $[Cat]_2[Mn^{II}Cl_4]$ salts were measured in several solvents (**Figure 3**).[44] In MeCN a deposition and a stripping of manganese can be observed for every salt tested. With $[EMP]^+$ and $[BMP]^+$ the current profiles look very similar. Mn deposition and stripping are separated by 0.87 and 0.95 V respectively. Additionally, two current maxima can be observed for the stripping, whereas only one current maximum is present with the $[N_{2225}]^+$ salt. Cations can influence the morphology of metal deposition,[37] thus the cations may be an explanation for the differing stripping behavior. However, with $[N_{2225}]^+$ the two processes are 1.26 V apart, making the $[EMP]^+$ and $[BMP]^+$ salt with lower overpotential more interesting. $[Mn^{II}Cl_4]^{2-}$- solutions in propylene carbonate (PC) and GBL only deposit, but do not strip manganese. Further Mn was deposited on Pt-foils (current density 0.25 mA cm^{-2}; 11.2 mA h = 11.3 mg Mn; Figure 3b). The Pt-foil is completely blank after the electrolysis in GBL, whereas a black layer was observed after deposition from MeCN.

© 2021 The Authors. Advanced Energy Materials published by Wiley-VCH GmbH

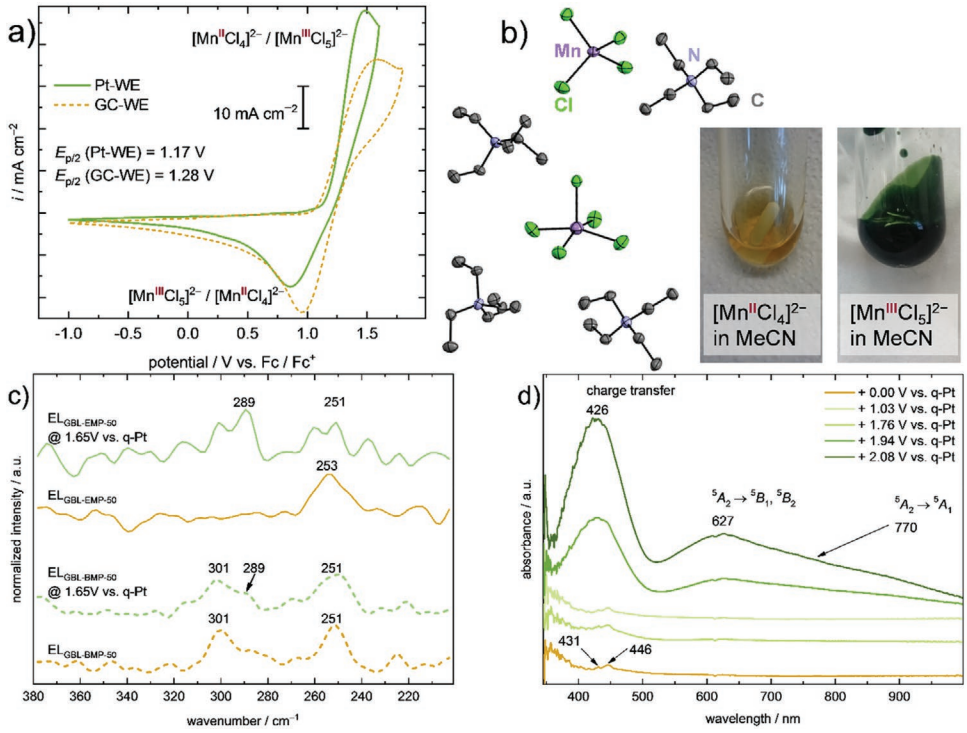

Figure 2. a) CV of $EL_{GBL\text{-}BMP\text{-}50}$ at a Pt-WE and a GC-WE with 100 mV s^{-1}. b) Molecular structure of the cocrystal $[NEt_4]_4[Mn^{II}Cl_4][Mn^{III}Cl_5]$, H-atoms and disorder of $[NEt_4]^+$ were omitted for clarity, thermal ellipsoids were drawn with 50% probability. Color of $[Mn^{II}Cl_4]^{2-}$ and $[Mn^{III}Cl_5]^{2-}$ dissolved in MeCN. c) Raman spectroelectrochemistry with $[EMP]_2[Mn^{II}Cl_4]$ in GBL (50 wt% GBL, $c = 1.4$ mol L^{-1}, $EL_{GBL\text{-}EMP\text{-}50}$) and $EL_{GBL\text{-}BMP\text{-}50}$. d) UV/Vis spectroelectrochemistry with $[BMP]_2[Mn^{II}Cl_4]$ in GBL (90 wt% GBL, $c = 0.22$ mol L^{-1}).

Apparently, $[Mn^{II}Cl_4]^{2-}$ is reduced at the electrode but the Mn metal formed does not stick to it. Figure 3b shows a typical photograph of an electrolyte after deposition in which the reduced Mn seems to end up as a black suspension. From MeCN, Mn deposition / stripping on a copper electrode was repeated 24 times with the respective voltage profiles / coulombic efficiency (CE) given in Figure 3c,d.

The CE slightly improves over the 24 cycles to still only 43%, probably due to the incomplete stripping of the mechanically unstable Mn layer that is formed. Thus, the photographs in Figure 3d demonstrate that the deposited Mn layer can easily be removed by washing the electrode with excess solvent. Note that manganese metal crystallizes in a unique elemental structure with 58 independent Mn atoms in the unit cell.[45] Apparently, Mn deposition on metal surfaces with closed-packed typical metal structures like Pt or Cu are a bad choice concerning the mechanical stability of the Mn film. To confirm that the black deposit is manganese, pXRD data of the black deposit powders on copper were recorded. **Figure 4**a shows the pXRD trace of a sample prepared under atmospheric conditions. The broad reflexes speak for an almost amorphous structure and fit very well to the pXRD of MnO instead of Mn, although the main reflex of α-manganese seems still to be present.[45,46] In the sample prepared under inert conditions (Figure 4b) MnO-reflexes are absent and the sample assigns as α-Mn. The oxidation of the deposited Mn to MnO under atmospheric conditions is expected and an indirect proof for the deposition of pure manganese under inert conditions (cf. Figure S9 (Supporting Information) for an EDX mapping). The SEM images of the deposited manganese films on different electrode materials always revealed a cauliflower like structure (see Figure 4), similar to the reported Mn deposits from non-aqueous media that delaminate very easily by washing the electrode.[35,36]

Before entering the huge field of Mn deposition, where temperature, deposition potential, additives and cations strongly influence the morphology of the deposited Mn films, we were satisfied with the fact that it is possible to deposit Mn from $[Mn^{II}Cl_4]^{2-}$ solutions and continued with first battery experiments, to check whether it is worth to return to Mn deposition later.

2.2.3. Linear Sweep Voltammetry (LSV)

LSV was used on a Mn-electrode to investigate, whether anodic dissolution is possible or hindered by passivation of the electrode surface, as often observed due to precipitation of insoluble species upon anodic dissolution in media with high chloride ion concentration.[47] Note that the chloride ion concentration in the Mn^0/Mn^{II}-half-cell will be high in the charged state. Since in GBL solutions of $[Cat]_2[Mn^{II}Cl_4]$ no stripping of Mn was observed (Mn^0-delamination? Figure 3b), the LSV of a solution of [EMP]Cl in GBL (1.9 mol L^{-1}) was recorded (Figure S12, Supporting Information). The anodic dissolution of Mn^0 starts at –0.65 V and does not show the typical current profile for a passivation, described in the literature.[47] Still at –0.45 and –0.2 V the current levels off for a short time, creating two plateaus. This is an

© 2021 The Authors. Advanced Energy Materials published by Wiley-VCH GmbH

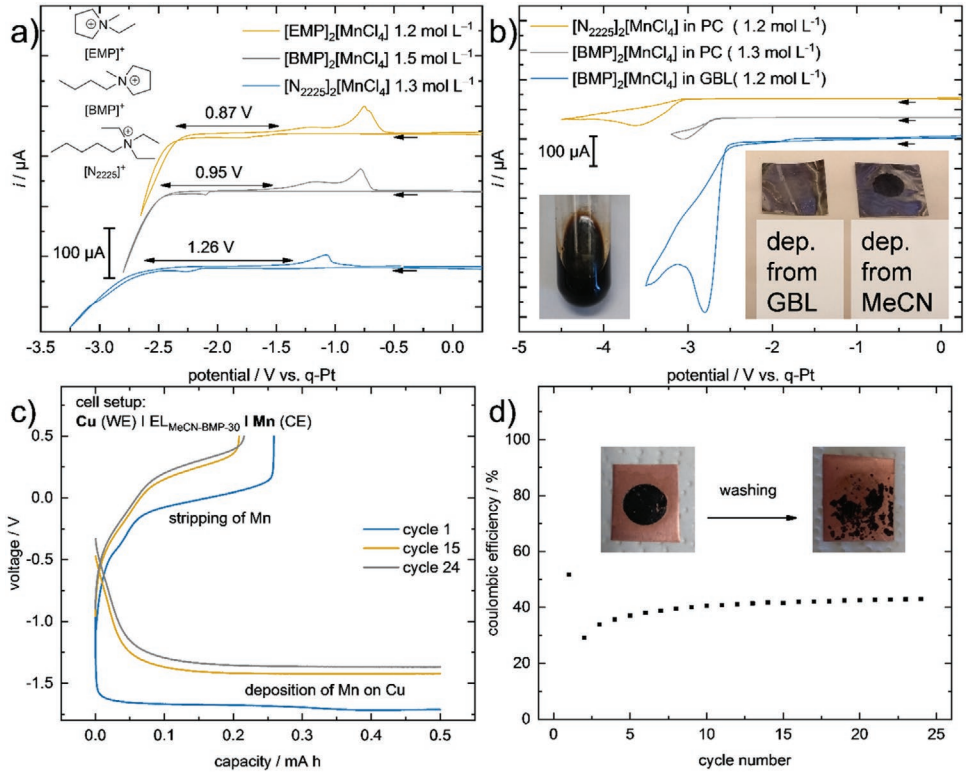

Figure 3. a) CVs of different $[Cat]_2[MnCl_4]$ salts in MeCN at a Pt-WE with a scan rate of 50 mV s^{-1}. b) CVs of different $[Cat]_2[MnCl_4]$ salts in PC and GBL at a Pt-WE with a scan rate of 50 mV s^{-1} plus photographs of Mn deposits from MeCN and GBL. c) Voltage profiles of the electrochemical deposition and stripping of Mn from a solution of $[BMP]_2[MnCl_4]$ in MeCN (1.6 mol L^{-1}, 30 wt% MeCN, $EL_{MeCN\text{-}BMP\text{-}30}$) using a Cu-electrode and a current density of 0.88 mA cm^{-2}. d) CE of the respective experiment plus photographs of the mechanically unstable Mn-layer (deposition of 2 mA h).

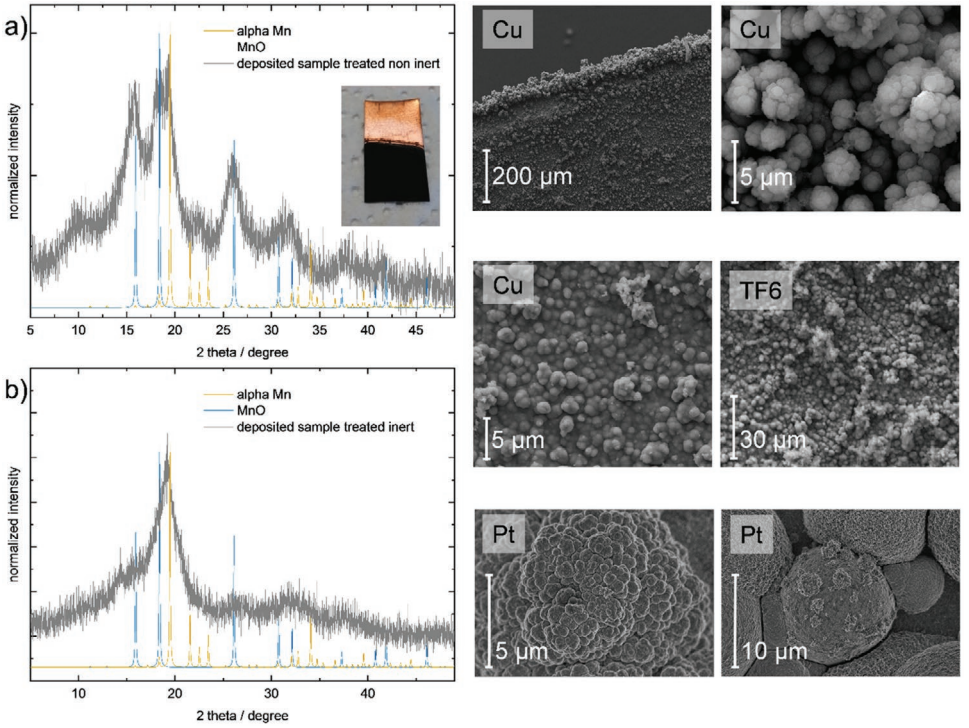

Figure 4. pXRD of manganese, deposited from $EL_{MeCN\text{-}BMP\text{-}30}$ on Cu a) handled under atmospheric conditions. b) Handled under inert conditions. SEM images of Mn deposits on Cu ($EL_{MeCN\text{-}BMP\text{-}30}$), TF6 ($EL_{MeCN\text{-}BMP\text{-}30}$) and Pt ($EL_{MeCN\text{-}BMP\text{-}Cl\text{-}30}$).

© 2021 The Authors. Advanced Energy Materials published by Wiley-VCH GmbH

indication that the anodic dissolution slows down for a moment, i.e., that the layer is not blocking the surface but just somewhat restricting flow. Since we are significantly away from the oxidation potentials for Mn^{III}, this suggests the system is not changing the oxidation state, but rather that the speciation changes as the metal concentration close to the electrode surface changes, e.g., $[Mn^{II}Cl_4]^{2-}$ could have a different solubility to a hypothetically formed ion $[Mn^{II}{}_2Cl_x]^{(4-x)}$ (x = 5–7) at the plateaus. Thus, the anodic dissolution of Mn is similar to the anodic dissolution of Zn or Sn.[47] Afterward the current increases further and indicates an almost unhindered dissolution of Mn^0. The final formation of the stable $[Mn^{II}Cl_4]^{2-}$ ion appears to be a very strong driving force, limiting the detrimental passivation.

2.2.4. Electrolytes

Table 1 summarizes the key parameters of the different electrolytes used throughout this work. Electrolyte optimizations (see the Supporting Information) revealed that the addition of extra [Cat]Cl to a solution of $[Cat]_2[Mn^{II}Cl_4]$ reduces the charge voltage (U_{SoC5}) by up to 0.62 V. Therefore, only electrolytes with [Cat]Cl as an additive were used for cycling experiments. Upon characterization of the BMP-GBL-electrolyte with 50 wt% GBL we observed that $[Mn^{II}Cl_4]^{2-}$ salts can precipitate, if the temperature drops. Thus, we decided to use 55 wt% GBL in the battery measurements and successfully prevented any precipitation. Although it was necessary to add more GBL (58 wt%) to dissolve all of the $[EMP]_2[MnCl_4]$ and [EMP]Cl ($EL_{GBL\text{-}EMP\text{-}Cl\text{-}58}$), its $[Mn^{II}Cl_4]^{2-}$ concentration is still higher compared to the $[BMP]^+$ based electrolyte with only 50 wt% of GBL ($EL_{GBL\text{-}BMP\text{-}Cl\text{-}50}$) (1.0 mol L^{-1} vs 0.9 mol L^{-1}).

MeCN-based electrolytes never showed any sign of precipitation even at a low solvent content of only 30 wt%, so we used these electrolytes for the characterization and the battery measurements. The acronyms used for the electrolytes EL include the solvent, the cation and the amount of solvent added to the salt in wt% in the subscript. This means, $EL_{GBL\text{-}BMP\text{-}50}$ stands for an electrolyte using $[BMP]_2[Mn^{II}Cl_4]$ as conducting salt and 50 wt% GBL as auxiliary solvent. If nothing is mentioned always Mn(II), i.e., $[Mn^{II}Cl_4]^{2-}$ is used. If Mn(III) is included with the subscript, the electrolyte contains $[Mn^{III}Cl_5]^{2-}$, e.g., $EL_{MeCN\text{-}BMP\text{-}Mn(III)\text{-}30}$. If "Cl" is included with the subscript, a 1:1 molar ratio of the cation chloride was added as in $EL_{MeCN\text{-}BMP\text{-}Cl\text{-}30}$ (cf. Table 1). An electrolyte marked with a * refers to an electrolyte, diluted with pure solvent to one half of the concentration of the active species.

2.2.5. Conductivity, Viscosity, and Ionicity

We investigated conductivity and viscosity of the all-MFB electrolytes based on $[BMP]_2[Mn^{II}Cl_4]$ and $[EMP]_2[Mn^{II}Cl_4]$ in GBL and MeCN. Both solvents have almost the same polarity (ε_{GBL} = 39.0; ε_{MeCN} = 36.64 at 25 °C), but differ in their viscosity (η_{GBL} = 1.738 cP; η_{MeCN} = 0.369 cP at 25 °C).[48,49] With respect to the diffusing entities, the larger $[BMP]^+$ ($V_{VdW,cat}$ 158 Å^3) and the smaller $[EMP]^+$ ($V_{VdW,cat}$ 124 Å^3) differ only slightly (chemical structures Figure S15, Supporting Information).[50] Overall, electrolytes based on more fluid MeCN and the smaller $[EMP]^+$ cation would be expected to perform better. Indeed, MeCN-electrolytes with $[EMP]^+$ showed the best conductivity and lowest viscosity of electrolytes tested (cf. Table 1). Therefore, and because it was the only solvent that allowed Mn film

Table 1. Abbreviations for the electrolytes used in this work and their physicochemical characteristics.

Electrolyte abbreviation[a)]	$[Cat]_2[MnCl_{4/5}]$	[Cat]Cl	$[Cat]_2[MnCl_4]$: [Cat]Cl (molar ratio)	Solvent [wt%]	c ($[MnCl_4]^{2-}$)/mol L^{-1}	Conductivity/mS cm^{-1} [T/°C]	Viscosity at 30 °C/cP
$EL_{GBL\text{-}BMP\text{-}50}$	$[BMP]_2[MnCl_4]$	–	–	GBL (50)	1.2	6.2 (30 °C)	13.9
$EL_{GBL\text{-}BMP\text{-}Mn(III)\text{-}50}$	$[BMP]_2[MnCl_5]$	–	–	GBL (50)	1.2	5.96 (30 °C)	14.6
$EL_{GBL\text{-}BMP\text{-}Cl\text{-}50}$	$[BMP]_2[MnCl_4]$	[BMP]Cl	1 : 1	GBL (50)	0.9	6.1 (31 °C)	14.9
$EL_{GBL\text{-}BMP\text{-}55}$	$[BMP]_2[MnCl_4]$	–	–	GBL (55)	1.1	6.08 (32 °C)	–
$EL_{GBL\text{-}BMP\text{-}Cl\text{-}55}$	$[BMP]_2[MnCl_4]$	[BMP]Cl	1 : 1	GBL (55)	0.8	6.07 (32 °C)	–
$EL_{GBL\text{-}BMP\text{-}Cl\text{-}55}{}^{*b)}$	$[BMP]_2[MnCl_4]$	[BMP]Cl	1 : 1	GBL (84)	0.4	–	–
$EL_{GBL\text{-}EMP\text{-}50}$	$[EMP]_2[MnCl_4]$	–	–	GBL (50)	1.4	8.59 (30 °C)	15.0
$EL_{GBL\text{-}EMP\text{-}Mn(III)\text{-}50}$	$[EMP]_2[MnCl_5]$	–	–	GBL (50)	1.3	9.46 (30 °C)	17.4
$EL_{GBL\text{-}EMP\text{-}Cl\text{-}58}$	$[EMP]_2[MnCl_4]$	[EMP]Cl	1 : 1	GBL (58)	1.0	10.57 (29 °C)	5.2
$EL_{GBL\text{-}EMP\text{-}Cl\text{-}58}{}^{*b)}$	$[EMP]_2[MnCl_4]$	[EMP]Cl	1 : 1	GBL (82)	0.5	–	–
$EL_{MeCN\text{-}BMP\text{-}30}$	$[BMP]_2[MnCl_4]$	–	–	MeCN (30)	1.6	12.6 (30 °C)	13.3
$EL_{MeCN\text{-}BMP\text{-}Mn(III)\text{-}30}$	$[BMP]_2[MnCl_5]$	–	–	MeCN (30)	1.5	9.22 (30 °C)	13.7
$EL_{MeCN\text{-}BMP\text{-}Cl\text{-}30}$	$[BMP]_2[MnCl_4]$	[BMP]Cl	1 : 1	MeCN (30)	1.1	11.7 (32 °C)	–
$EL_{MeCN\text{-}BMP\text{-}Cl\text{-}30}{}^{*b)}$	$[BMP]_2[MnCl_4]$	[BMP]Cl	1 : 1	MeCN (74)	0.55	–	–
$EL_{MeCN\text{-}EMP\text{-}50}$	$[EMP]_2[MnCl_4]$	–	–	MeCN (50)	1.2	30.1 (32 °C)	2.3
$EL_{MeCN\text{-}EMP\text{-}Mn(III)\text{-}50}$	$[EMP]_2[MnCl_5]$	–	–	MeCN (50)	1.1	30.6 (30 °C)	2.2

[a)]The electrolytes with the highest concentrations in Table 2 are close to the maximal concentration of the respective combination of salt and solvent; [b)]Electrolyte, diluted with pure solvent to one half of the concentration of the active species.

© 2021 The Authors. Advanced Energy Materials published by Wiley-VCH GmbH

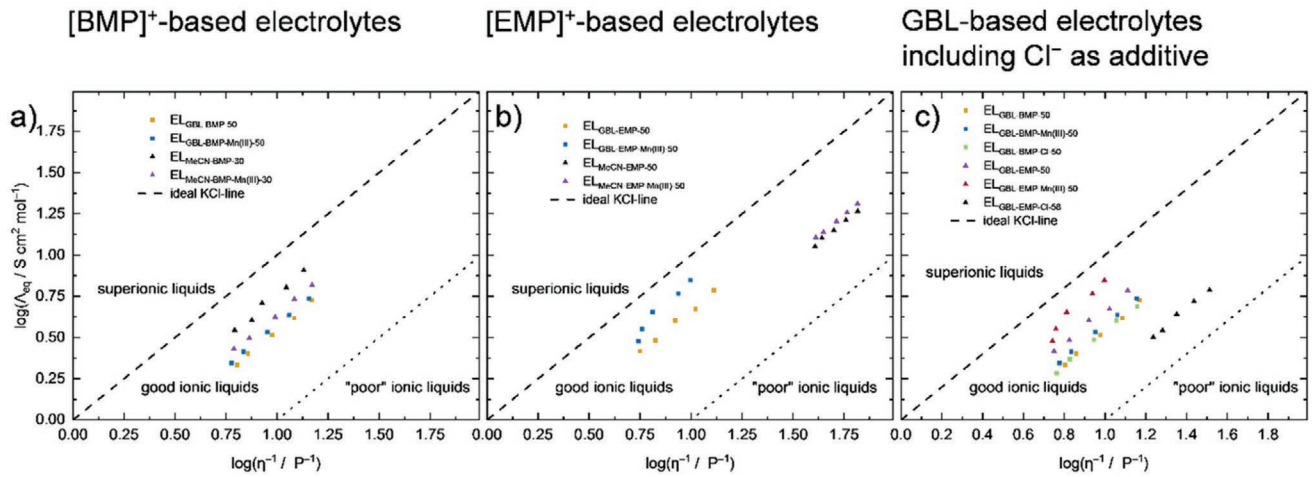

Figure 5. Walden plots for a) $EL_{GBL\text{-}BMP\text{-}50}$, $EL_{GBL\text{-}BMP\text{-}Mn(III)\text{-}50}$, $EL_{MeCN\text{-}BMP\text{-}30}$ and $EL_{MeCN\text{-}BMP\text{-}Mn(III)\text{-}30}$; b) $EL_{GBL\text{-}EMP\text{-}50}$, $EL_{GBL\text{-}EMP\text{-}Mn(III)\text{-}50}$, $EL_{MeCN\text{-}EMP\text{-}50}$ and $EL_{MeCN\text{-}EMP\text{-}Mn(III)\text{-}50}$, and c) $EL_{GBL\text{-}BMP\text{-}50}$, $EL_{GBL\text{-}BMP\text{-}Mn(III)\text{-}50}$, $EL_{GBL\text{-}BMP\text{-}Cl\text{-}50}$, $EL_{GBL\text{-}EMP\text{-}50}$, $EL_{GBL\text{-}EMP\text{-}Mn(III)\text{-}50}$, and $EL_{GBL\text{-}EMP\text{-}Cl\text{-}58}$.

formation during deposition, we decided to further use MeCN, despite not being desirable for a battery application. The alternative solvent GBL, was already used in Lithium ion batteries (LIBs) and is well-known for its low flammability and great electrochemical stability.[51–53] Figure S15 (Supporting Information) shows the Arrhenius plots of the ionic conductivity and viscosity of the $[BMP]^+$ and $[EMP]^+$ salts in GBL and MeCN. High ionic conductivity of the electrolyte is important at any state of charge (SoC). Thus, the corresponding $[Mn^{III}Cl_5]^{2-}$-salts, that dominate the ionic conductivity at higher SoCs, were also analyzed (Figure S15, Supporting Information). Comparing the for the battery cycling relevant electrolytes $EL_{MeCN\text{-}BMP\text{-}30}$ and $EL_{GBL\text{-}BMP\text{-}50}$ with similar viscosity (13.3 vs 13.9 cP), the doubled conductivity in MeCN (12.6 vs 6.2 mS cm^{-1} in GBL) in part originates from the higher concentration of $[BMP]_2[Mn^{II}Cl_4]$ accessible in MeCN (1.6 mol L^{-1} vs 1.2 mol L^{-1}). But apparently this does not reflect the entire change. Further insight is gained from a "Walden plot" (**Figure 5**), where $\ln(\Lambda_m)$ is plotted against $\ln(\eta)$. Because $[Cat]_2[Mn^{II}Cl_4]$ is a 2:1-salt we used the equivalent conductivity (Λ_{eq}) instead of the molar conductivity (Λ_m), otherwise a comparison to the ideal KCl-line would not be valid. In the Walden plot basing on Walden's rule Equation (4)

$$\Lambda_m \eta = \text{constant} \quad (4)$$

the location of the electrolyte compared to the ideal KCl-line is relevant. If an electrolyte lies on the ideal KCl-line, all ions are fully dissociated, move independently and contribute maximal to the ionic conductivity.[54] The further apart from the KCl-line the electrolyte, the more ion-pairing takes place. Comparing the $[BMP]^+$ salts in GBL and MeCN, the data points for $EL_{MeCN\text{-}BMP}$ are closer to the ideal KCl-line than $EL_{GBL\text{-}BMP}$. This higher ionicity of $EL_{MeCN\text{-}BMP}$ presumably contributes to their better conductivity in addition to their higher concentration. By contrast, the $[EMP]^+$ salts are more soluble in GBL than in MeCN, i.e., 1.4 mol L^{-1} versus 1.2 mol L^{-1}. Still the $EL_{MeCN\text{-}EMP}$ conductivity is much better than that of $EL_{GBL\text{-}EMP}$, apparently due to the much lower viscosity of the electrolytes with MeCN, e.g., $EL_{MeCN\text{-}EMP\text{-}50}$ at 2.3 versus 12.6 cP for $EL_{GBL\text{-}EMP\text{-}50}$ both containing 50 wt% solvent (cf. Table 1). Notably, the $EL_{MeCN\text{-}EMP\text{-}50}$ conductivity reaches more than 30 mS cm^{-1} for a 1.2 M solution. This is about three times higher than that of the optimized LP 30 LIB electrolyte (10.25 mS cm^{-1} @ 1.0 mol L^{-1} $Li[PF_6]$ in EC/DMC 1:1).[55] According to the Walden plots in Figure 5, the $[EMP]^+$ salts have a lower ionicity in MeCN than in GBL. Although $[BMP]^+$ and $[EMP]^+$ are structurally rather similar, the small volume difference of 34 $Å^3$ or 22% for $[EMP]^+$ results in huge changes toward the electrochemical properties of the electrolytes. Thus, tailor-made $[Mn^{II}Cl_4]^{2-}$ salts could further lift a great potential for optimized electrolyte properties. So far, $EL_{GBL\text{-}EMP\text{-}50}$ is the best candidate, just considering the ionicity. Referring to viscosity and conductivity $EL_{MeCN\text{-}EMP\text{-}50}$ exceeds the other electrolytes. Overall, $EL_{GBL\text{-}BMP\text{-}50}$ and $EL_{MeCN\text{-}BMP\text{-}30}$ are reasonable compromises concerning ionicity, conductivity, viscosity, and the availability of [Cat]Cl (where [BMP]Cl is quite a bit cheaper than [EMP]Cl).

Figure 5c also includes the electrolytes with additional [Cat]Cl in GBL. All electrolytes with $[EMP]_2[Mn^{II}Cl_4]$ in GBL show higher conductivity than the electrolytes with $[BMP]^+$. In the Walden plot, the $[EMP]^+$-based electrolyte with additional [EMP]Cl is further away from the ideal KCl-line as any of the $[BMP]^+$ based electrolytes. Therefore, we decided to analyze the $[BMP]^+$ salts more detailed because of the higher ionicity and the better comparability to the $EL_{MeCN\text{-}BMP\text{-}Cl\text{-}30}$. Besides, the conductivity of $EL_{GBL\text{-}BMP\text{-}Cl\text{-}50}$ (6.1 mS cm^{-1} at 31 °C) still lies at the bottom of the range of liquid electrolytes used in LIBs.[56] After the detailed electrochemical measurements with $EL_{GBL\text{-}BMP\text{-}Cl\text{-}50}$ we also performed a cycling experiment with more conducting $EL_{GBL\text{-}EMP\text{-}Cl\text{-}58}$ (10.57 mS cm^{-1} at 29 °C) to evaluate the differences.

2.3. Investigations in Static Battery Cells

For the identification of a suitable battery setup and first investigations of the different electrolytes, battery cycling experiments were performed in static cells with the FAPQ-375-PP AEM and the optimized electrolytes (Supporting Information). Additionally, the static cells need only 1.04 mL of electrolyte. In the flow cell, a minimum of 20 mL is needed just to fill the cell and the tubing, allowing to save material for orientation.

© 2021 The Authors. Advanced Energy Materials published by Wiley-VCH GmbH

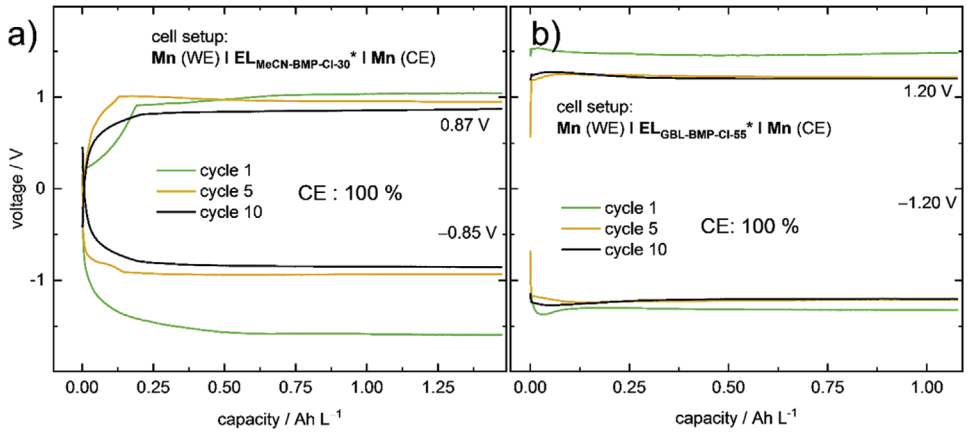

Figure 6. Half-cell experiments with a) $EL_{MeCN-BMP-Cl-30}$* using a Mn-WE and a Mn-CE d) $EL_{GBL-BMP-Cl-55}$* using a Mn-WE and a Mn-CE. All experiments were conducted with a current density of 0.25 mA cm^{-2}.

2.3.1. Half-Cell Experiments on Mn Deposition

To further investigate the deposition of manganese from $EL_{GBL-BMP-Cl-55}$* and $EL_{MeCN-BMP-Cl-30}$* half-cell experiments were conducted (**Figure 6**). Symmetrical cells with Mn^0 electrodes were built delivering an overpotential for the stripping and the deposition of Mn in $EL_{MeCN-BMP-Cl-30}$* that lies between 0.85 and 0.87 V. Since Mn is deposited on one electrode and stripped from the other, it is not possible to split the overpotential in a part for deposition and another part for stripping. Theoretically, both processes can be kinetically hindered. In the corresponding asymmetrical cell, where Mn was deposited on a Pt electrode, the potential for the Mn deposition on Pt and the simultaneous stripping of Mn is in the same region yielding +0.88 V (see Figure S22, Supporting Information). Since the Mn electrodes act as huge Mn reservoirs, the Mn|Mn-half-cell shows a CE of 100% over 10 cycles. Nevertheless, also this electrolyte does transform to a black suspension, due to "dead" manganese, showing that no stable Mn layer is formed during the deposition. At least, it clearly demonstrates that—favorably—the stripping of Mn takes place. $EL_{GBL-BMP-Cl-55}$* yields an even larger overpotential of 1.20 V for Mn deposition and stripping (Figure 6). The difference to $EL_{MeCN-BMP-Cl-30}$* is 0.33–0.35 V, which is also the difference between U_{SoC5} of respective full-cells measured with Pt electrodes (see Figure S16, Supporting Information). This could be a first hint that the measured overpotential is solely caused by the deposition of Mn, since anodic dissolution of Mn does not take place, while charging a full-cell. This is further supported by the LSV experiment (Figure S12, Supporting Information), which showed that the anodic dissolution of Mn is not hindered by any passivating effects. Although the conductivity of $EL_{MeCN-BMP-Cl-30}$ is almost twice as large as the conductivity of $EL_{GBL-BMP-Cl-55}$ at 32 °C (11.7 mS cm^{-1} vs 6.07 mS cm^{-1}), its influence on U_{SoC5} seems to be negligible.

2.3.2. Electrochemical Investigations of the $Mn^{II}|Mn^{III}$-Half-Cell

Unfortunately, we did not find a suitable half-cell experiment for the $Mn^{II}|Mn^{III}$-half-cell due to the lack of a suitable counter electrode. To learn more about the reversibility of the $[Mn^{II}Cl_4]^{2-}$/$[Mn^{III}Cl_5]^{2-}$ redox couple and the stability of $[Mn^{III}Cl_5]^{2-}$, **Figure 7** shows the CV of $EL_{GBL-BMP-50}$ with the current response of the $[Mn^{II}Cl_4]^{2-}$/$[Mn^{III}Cl_5]^{2-}$ couple at different scan rates ($c = 1.2$ mol L^{-1}; no supporting electrolyte).[57] Thus, the ratio of the cathodic and the anodic peak currents (i_{pc} and i_{pa}) was evaluated

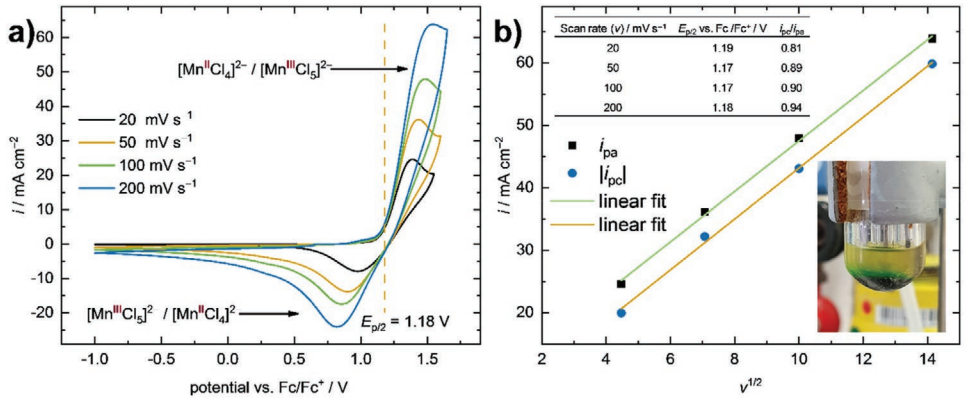

Figure 7. a) CV of $EL_{GBL-BMP-50}$ using a 1 mm Pt disc working electrode at different scan rates. b) Dependency of the peak currents (i_{pa} and i_{pc}) from the square root of the scan rate, independency of $E_{p/2}$ from the scan rate and a photograph of the CV cell after analyzing the $[Mn^{II}Cl_4]^{2-}$/$[Mn^{III}Cl_5]^{2-}$ redox couple, that shows the formation of a $[Mn^{III}Cl_5]^{2-}$ rich layer at the bottom of the cell due to its higher density.

© 2021 The Authors. Advanced Energy Materials published by Wiley-VCH GmbH

for battery performance as it displays the possibility, if all of the electrochemically formed $[Mn^{III}Cl_5]^{2-}$ ions could be reduced. The ratio can be compared to the CE in a battery measurement, with a ratio of one being equivalent to a CE of 100% (Figure 7).

For the $[Mn^{II}Cl_4]^{2-}/[Mn^{III}Cl_5]^{2-}$ redox couple the i_{pa}/i_{pc} ratio increases from 0.81 to 0.94 with increasing scan rate. The i_{pa}/i_{pc} ratios were calculated according to Equation S8 (Supporting Information). This implies that 94% of the $[Mn^{III}Cl_5]^{2-}$ ions are again reduced to $[Mn^{II}Cl_4]^{2-}$ at a scan rate of 200 mV s^{-1}. At a scan rate of 20 mV s^{-1} this value is lower with 81%. This complies with the observation that the intense green coloration of the $[Mn^{III}Cl_5]^{2-}$ ion at the working electrode during the anodic scan moves away from the electrode through convection (Figure 7b) and suggests an increased density of the $[Mn^{III}Cl_5]^{2-}$ rich layer formed at the electrode. As a result, $[Mn^{III}Cl_5]^{2-}$ ions leave the diffusion layer in front of the electrode and are no longer available for the reduction to $[Mn^{II}Cl_4]^{2-}$ during the reverse scan. This behavior also explains why the i_{pa}/i_{pc} ratio is closer to one at faster scan rates, since the available time for the $[Mn^{III}Cl_5]^{2-}$ anion to leave the diffusion layer at the electrode is drastically lowered.[58] Yet, the $E_{p/2}$ versus Fc/Fc^+ of the $[Mn^{II}Cl_4]^{2-}/[Mn^{III}Cl_5]^{2-}$ couple at 1.18±0.01 V are independent from the scan rate and the peak currents (i_p) are proportional to the square root of the scan rate and indicate electrochemical reversibility (Figure 7). Since 94% of $[Mn^{III}Cl_5]^{2-}$ can be reduced at a scan rate of 200 mV s^{-1} and a clear trend toward an i_{pa}/i_{pc} ratio of one follows for increasing scan rates, the electrochemical reversibility of the $[Mn^{II}Cl_4]^{2-}/[Mn^{III}Cl_5]^{2-}$ redox couple is sufficient for the battery. In addition, the convection of the $[Mn^{III}Cl_5]^{2-}$ becomes irrelevant in a flow-cell, since a mixing of the electrolyte occurs in the storage tank and therefore, the availability of $[Mn^{III}Cl_5]^{2-}$ at the electrode during discharge of the battery is guaranteed at any time.

2.3.3. Electrode Material for the Positive Electrode

Due to its inertness and the possibility to combine it with felt electrodes, graphite is a very commonly used, economical inert electrode material used in the VRFB. But is it applicable as the positive electrode in the all-MFB? To keep the system during initial testing as simple as possible, planar plate electrodes were preferred over porous felt electrodes, given the caveat that higher current densities will not be achieved. **Figure 8** shows full cell cycling experiments to evaluate the hard-carbon TF6. Mn plates were used as counter electrodes, to ensure that enough Mn is available at any time to be oxidized during discharge.

For the $EL_{GBL\text{-}BMP\text{-}Cl\text{-}55}/EL_{GBL\text{-}BMP\text{-}Cl\text{-}55}$* cell U_{SoC5} is almost the same, regardless whether a TF6- or a Pt electrode is used. In both cases, a higher U_{SoC5} was observed during the first cycle compared to the 5th and 10th cycle. We attribute this to Mn deposition, since the same phenomenon was observed in the Mn|Mn-half-cells (Figure 6). However, a significant difference occurs in the voltage profiles of the discharge plateaus. Only one plateau was observed using TF6 as the positive electrode, which is exactly to be expected for a battery with one reversible electrochemical process at each electrode. With Pt used as the positive electrode, two clearly separated plateaus appeared, indicating that two different electrochemical processes took place

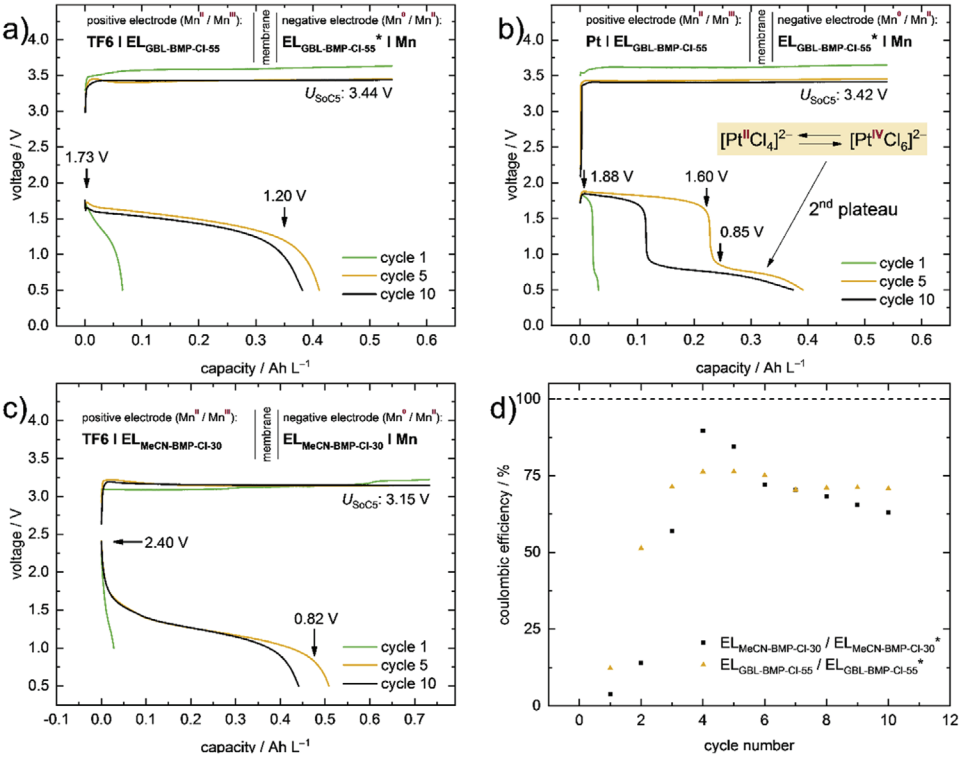

Figure 8. Cycling experiment with $EL_{GBL\text{-}BMP\text{-}Cl\text{-}55}/EL_{GBL\text{-}BMP\text{-}Cl\text{-}55}$* and a current density of 0.25 mA cm^{-2} a) using a graphite-WE (TF6) and a Mn-CE. b) Using a Pt-WE and a Mn-CE. c) Cycling experiment with $EL_{MeCN\text{-}BMP\text{-}Cl\text{-}30}/EL_{MeCN\text{-}BMP\text{-}Cl\text{-}30}$ and a current density of 0.5 mA cm^{-2} using a graphite-WE (TF6) and a Mn-CE. d) Coulombic efficiencies of the batteries described in (a) and (c).

© 2021 The Authors. Advanced Energy Materials published by Wiley-VCH GmbH

during discharge. Since the negative electrode is exactly the same for both experiments these processes have to be located at the Pt electrode. We found that the Pt electrode is non-innocent under these conditions and reacts to give $[Pt^{II}Cl_4]^{2-}$ and $[Pt^{IV}Cl_6]^{2-}$. Thus, next to the reduction of $[Mn^{III}Cl_5]^{2-}$, $[Pt^{IV}Cl_6]^{2-}$ is reduced to $[Pt^{II}Cl_4]^{2-}$ during discharge, which is responsible for the 2nd plateau (see the Supporting Information for an extended section). However, with TF6 as electrode material, the intended cell reactions proceed, which means that it is suitable as electrode material and was therefore used in the following experiments. The CE of the TF6|Mn-full-cell reaches a plateau 70%, during the last four cycles. With Mn as negative electrode a CE of 100% should be expected, since the $[Mn^{II}Cl_4]^{2-}/[Mn^{I-II}Cl_5]^{2-}$ redox couple is completely reversible. This means that the reduced CE has to originate from elsewhere. $EL_{MeCN\text{-}BMP\text{-}Cl\text{-}30}$ shows a slightly reduced CE compared to the respective cell with $EL_{GBL\text{-}BMP\text{-}Cl\text{-}55}/EL_{GBL\text{-}BMP\text{-}Cl\text{-}55}$*. However, U_{SoC5} is advantageously reduced by 0.29 V in the cell with $EL_{MeCN\text{-}BMP\text{-}Cl\text{-}30}$.

2.3.4. Effect of EL-Concentration on Cycling

In the cell with $EL_{MeCN\text{-}BMP\text{-}Cl\text{-}30}$ (Figure 8), the same concentration of $[Mn^{II}Cl_4]^{2-}$ was used in both half cells. Since Mn deposition is a 2 e^- process and $[Mn^{II}Cl_4]^{2-}$ oxidation a 1 e^- process, $EL_{GBL\text{-}BMP\text{-}Cl\text{-}55}$* was used at the negative electrode, containing only half of the $[Mn^{II}Cl_4]^{2-}$ concentration compared to $EL_{GBL\text{-}BMP\text{-}Cl\text{-}55}$, used at the positive electrode.[59] Figure S26 (Supporting Information) shows a similar cycling experiment of a cell with $EL_{MeCN\text{-}BMP\text{-}Cl\text{-}30}$* at the negative electrode. Yet, using $EL_{MeCN\text{-}BMP\text{-}Cl\text{-}30}$* at the negative electrode resulted in a strong decrease of the CE. Over ten cycles the CE was between 12% and 22%, whereas in the cell with $EL_{MeCN\text{-}BMP\text{-}Cl\text{-}30}$ in both half cells the CE reached a plateau at 63%. This is a reduction of more than 40% compared to the cell presented in Figure 8. Apparently, $EL_{MeCN\text{-}BMP\text{-}Cl\text{-}30}$* has such a decreased viscosity compared to $EL_{MeCN\text{-}BMP\text{-}Cl\text{-}30}$, that the self-discharge through leaching is accelerated and leads to the observed decrease of the CE. Figure S27 (Supporting Information) shows the voltage profile and the CE of a cell with $EL_{GBL\text{-}BMP\text{-}Cl\text{-}55}$ in both half cells. Compared to the cell with $EL_{GBL\text{-}BMP\text{-}Cl\text{-}55}$ at the positive and $EL_{GBL\text{-}BMP\text{-}Cl\text{-}55}$* at the negative electrode (Figure 8) the CE is slightly higher. This further supports the assumption that a reduced viscosity of the electrolyte promotes leaching. But since the GBL based electrolytes are more viscous than the MeCN based electrolytes the effect is much weaker there, which might be an additional advantage of GBL with respect to MeCN.

2.3.5. Electrode Material for the Negative Electrode

Only the unfavorable deposition of Mn on various metal electrodes leading to either a mechanically unstable Mn film or no film at all were hitherto found. Therefore, we investigated graphite as a material for the negative electrode. From LIB work it is known that Mn deposition takes place on graphite, although it is not favored in this case.[60] In the next section only $EL_{GBL\text{-}BMP\text{-}Cl\text{-}55}/EL_{GBL\text{-}BMP\text{-}Cl\text{-}55}$* will be used to analyze the TF6|TF6 versus a TF6|Mn-full-cell cycling in **Figure 9**. U_{SoC5} decreases by 0.41 V compared to the full-cell with Mn as negative electrode, whereas the CE shows the same trend and reaches a plateau at 75% (Figure S28, Supporting Information). Unfortunately, the corresponding half-cell experiment for the deposition of Mn shows that unclear electrochemical reactions take place at the TF6 electrode during charging and discharging. Although a distinct voltage plateau is reached in the first cycle during the presumed deposition of Mn on TF6, an extreme drop in the charge voltage occurred at the beginning of the 5th and the 10th cycle. This was not observed in any other half-cell experiment so far and may be assigned to an alteration of the TF6 material during cycling. The photographs of the TF6 plate after cell-disassembly (Figure 9 and Figure S29: Supporting Information) prove this alteration. Upon charging the battery the electrolyte cations may intercalate into the TF6 material accompanied by electroreduction of the graphite. Upon battery discharge, the cations are removed leaving behind a strongly altered graphite surface. Possibly this facilitates intercalation in the next charge/discharge steps and may account for the drop in the charge voltage in the 5th and 10th cycle of the half-cell experiment.

Since Mn deposition is favored on graphite materials rather than the intercalation of Mn^{2+} ions, the intercalation of $[BMP]^+$ is suggested.[61,62,63] Intercalation into the TF6 material is

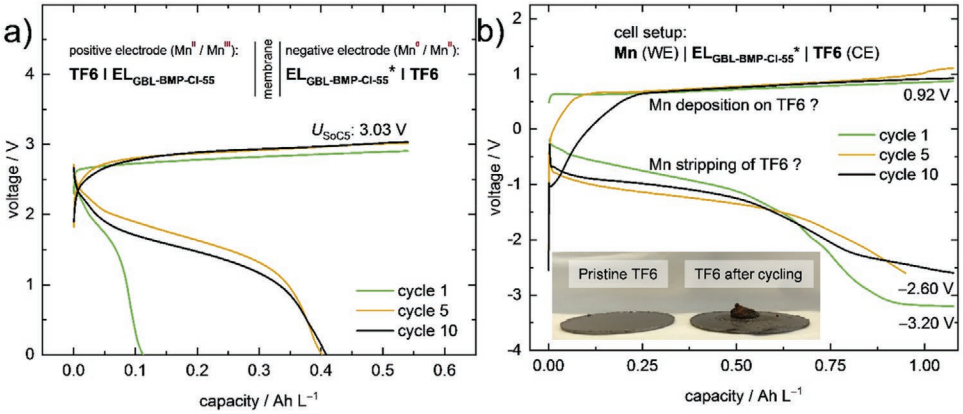

Figure 9. a) Full-cell cycling experiment with $EL_{GBL\text{-}BMP\text{-}Cl\text{-}55}/EL_{GBL\text{-}BMP\text{-}Cl\text{-}55}$* using a TF6 counter and working electrode. b) Half-cell experiment with $EL_{GBL\text{-}BMP\text{-}Cl\text{-}55}$* using a Mn working and a TF6 counter electrode. For both experiments a current density of 0.25 mA cm^{-2} was used.

© 2021 The Authors. Advanced Energy Materials published by Wiley-VCH GmbH

further supported by the voltage profiles of the half-cell experiment that should belong to the stripping of manganese. No clear plateau is distinguishable. The voltage slowly decreases until it reaches −3.20 V in the first cycle. At this voltage the oxidation of $[Mn^{II}Cl_4]^{2-}$ should already take place and probably does. On the other hand, the SEM image of the Mn deposition on TF6 looks very similar to the images for the deposition on Cu and Pt. It is therefore also possible that Mn deposition takes place and the alteration of the TF6 surface is caused by another effect via an interaction of the TF6 material at negative potentials with the solvent. CV experiments with the electrochemically inert supporting electrolyte $[NBu_4][PF_6]$ (see Figure S30, Supporting Information) demonstrate that the TF6 surface is altered strongly at negative potentials, supporting the argument for intercalation of $[BMP]^+$ in a reduced TF6 electrode material.

2.3.6. SoC 80 Cycling

Previously, all cycling experiments to identify the most promising battery setup only aimed at a SoC of 5% to save time. With the large volume of the setup, the high energy content of the electrolytes and the low current density of 0.25 mA cm^{-2}, applicable with the planar electrodes, charging to SoC5 already took 2.4 h, while going to SoC100 (10.75 Ah L^{-1}) would take 47.1 h. After identifying our most promising static battery, the TF6|Mn-cell with $EL_{GBL\text{-}BMP\text{-}Cl\text{-}55}/EL_{GBL\text{-}BMP\text{-}Cl\text{-}55}$*, cycling between a SoC of 0 and 80% was performed. **Figure 10** shows the voltage profiles of the corresponding battery experiment.

When charging from SoC5 to SoC80, the voltage slowly rises by 0.25 V and reaches an U_{SoC80} of 3.69 V after the first cycle (Figure 10), apparently induced by overpotentials during Mn deposition. In the following cycles U_{SoC80} increased further from 3.69 to 3.98 V in the 7th cycle and later the cycling stopped by reaching the voltage limit of 4 V. In addition, Figure S25 (Supporting Information) shows that the cell resistance during the deposition of Mn increased from 77 to 143 Ω. Both may be attributed to the reduced Mn^0-particles that do not stick to the electrode surface and potentially block the pores of the membrane preventing the necessary charge transport. The CEs reduced to 16% and 35%, significantly lower compared to the SoC5 cycling experiment with CEs around 70% and probably due to serious self-discharge by $[Mn^{III}Cl_5]^{2-}$ leaching. More pronounced for SoC80, because one cycle takes 2.4 h for SoC5 but 37 h for SoC80. Apparently, through increased cell resistance and Mn^{III}-leaching the lower cut-off voltage is reached prior to full battery discharge. Secondary evidence stems from the intensely green-colored electrolyte (→ Mn^{III}) withdrawn from the Mn^{II}/Mn^{III}-half-cell, although the battery was disassembled presumably discharged with a cut-off voltage of 0.5 V reached.

2.3.7. Full Cell Battery Measurements with $[EMP]_2[Mn^{II}Cl_4]$ in GBL

Since the electrolyte with $[EMP]_2[Mn^{II}Cl_4]$ and [EMP]Cl in GBL ($EL_{GBL\text{-}EMP\text{-}Cl\text{-}58}/EL_{GBL\text{-}EMP\text{-}Cl\text{-}58}$*) has higher conductivity, lower viscosity, but also lower ionicity than $EL_{GBL\text{-}BMP\text{-}Cl\text{-}55}/EL_{GBL\text{-}BMP\text{-}Cl\text{-}55}$*, it appeared interesting to be used for a last static test series. Figure S31 (Supporting Information) shows the voltage profiles (SoC5) of the respective battery measurements and the corresponding CEs. Although U_{SoC5} is the same, the discharge plateau of the battery with $EL_{GBL\text{-}EMP\text{-}Cl\text{-}58}/EL_{GBL\text{-}EMP\text{-}Cl\text{-}58}$* is reduced by around 0.18 V. In addition, the OCV at SoC80 is reduced by 0.26 V compared to the cell with the $EL_{GBL\text{-}BMP\text{-}Cl\text{-}55}/EL_{GBL\text{-}BMP\text{-}Cl\text{-}55}$*. More drastic is the decrease of the CE, which is reduced around 40%. All these observations agree with the leaching of $[Mn^{III}Cl_5]^{2-}$ into the Mn^0/Mn^{II}-half-cell. Due to the much higher fluidity of $EL_{GBL\text{-}EMP\text{-}Cl\text{-}58}$ compared to $EL_{GBL\text{-}EMP\text{-}Cl\text{-}50}$ (5.8 vs 17.2 cP), this process is more dominant in $EL_{GBL\text{-}EMP\text{-}Cl\text{-}58}$ cells. Cycling between SoC0 and SoC80 with $EL_{GBL\text{-}EMP\text{-}Cl\text{-}58}/EL_{GBL\text{-}EMP\text{-}Cl\text{-}58}$* yielded a CE below 5%, which agrees with the further accelerated Mn^{III}-leaching in the more fluid electrolyte. Yet, the lower ionicity of $EL_{GBL\text{-}EMP\text{-}Cl\text{-}58}/EL_{GBL\text{-}EMP\text{-}Cl\text{-}58}$* does not influence the battery measurement.

2.4. Energy Density of All-MFB Electrolytes from Static Measurements

The practical energy densities realized for the all-MFB were investigated. For the theoretical specific capacities (C_s^{th}) of each half-cell (Equation (S2) Supporting Information) the only variable

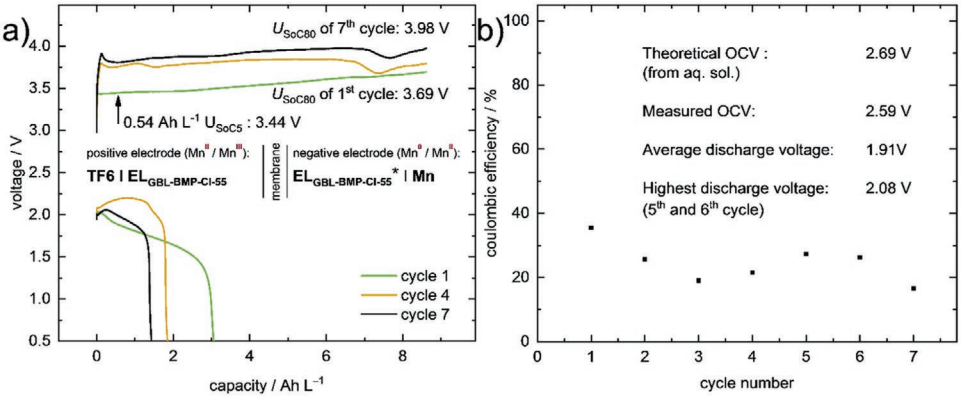

Figure 10. a) Voltage profiles of the TF6|Mn^0-full-cell with $EL_{GBL\text{-}BMP\text{-}Cl\text{-}55}/EL_{GBL\text{-}BMP\text{-}Cl\text{-}55}$* cycled between SoC0 and SoC80 with a current density of 0.25 mA cm^{-2}. The cycling between SoC0 and SoC80 was performed directly after the cycling between SoC0 and SoC5 with the same battery cell. b) Corresponding CEs and relevant parameters for the calculation of the energy density.

© 2021 The Authors. Advanced Energy Materials published by Wiley-VCH GmbH

Table 2. Specific capacities (C_s) and energy densities (W_s) of different electrolytes tested throughout this work with a cell potential (E_{cell}) of 2.59 V.

Electrolyte		$c([Mn^{II}Cl_4]^{2-})$/mol L^{-1}		C_s/Ah L^{-1}		$C_{s,\,total}$/Ah L^{-1} [e]	$W_s(E_{cell} = 2.59\ V)$/[Wh L^{-1}]
Negative electrode[a]	Positive electrode[b]	Anolyte[c]	Catholyte[d]	Anol.	Cathol.	Anol. + Cathol.	Overall
$EL_{GBL\text{-}BMP\text{-}50}$	$EL_{GBL\text{-}BMP\text{-}50}$	1.2	1.2	64.3	32.2	21.4	55.5
$EL_{GBL\text{-}BMP\text{-}Cl\text{-}55}$	$EL_{GBL\text{-}BMP\text{-}Cl\text{-}55}$	0.8	0.8	42.9	21.4	14.3	37.0
$EL_{GBL\text{-}BMP\text{-}Cl\text{-}55}$	$EL_{GBL\text{-}BMP\text{-}Cl\text{-}55}$*	0.4	0.8	21.4	21.4	10.7	27.8
$EL_{MeCN\text{-}BMP\text{-}30}$	$EL_{MeCN\text{-}BMP\text{-}30}$	1.6	1.6	85.8	42.9	28.6	74.0
$EL_{MeCN\text{-}BMP\text{-}Cl\text{-}30}$	$EL_{MeCN\text{-}BMP\text{-}Cl\text{-}30}$	1.1	1.1	59.0	29.5	19.7	50.9
$EL_{GBL\text{-}EMP\text{-}50}$	$EL_{GBL\text{-}EMP\text{-}50}$	1.4	1.4	75.0	37.5	25.0	64.8
$EL_{GBL\text{-}EMP\text{-}Cl\text{-}58}$	$EL_{GBL\text{-}EMP\text{-}Cl\text{-}58}$	1.0	1.0	53.6	26.8	17.9	46.3

[a]Mn^0/Mn^{II}-half-cell; [b]Mn^{II}/Mn^{III}-half-cell; [c]anolyte = electrolyte at the negative electrode; [d]catholyte = electrolyte at the positive electrode; [e]Since a two-electron process takes place at the negative electrode, whereas a one-electron process is present at the positive electrode, the amount of anolyte is cut by half compared to the amount of catholyte. This has to be considered, when calculating the capacity ($C_{s,\,total}$) for the entire system. $C_{s,\,total}$ in Ah L^{-1} is one third of C_s for the anolyte, or two thirds of C_s for the catholyte.

is the active Mn^{II} concentration. **Table 2** shows their influence on C_s^{th}. For $[BMP]_2[Mn^{II}Cl_4]$ with MeCN ($EL_{MeCN\text{-}BMP\text{-}30}$) the largest, currently observed concentration of Mn^{II} (1.6 mol L^{-1}) was obtained. Yet, the addition of [Cat]Cl leads to a reduction of C_s^{th} from 21.4 to 14.3 Ah L^{-1} going from $EL_{GBL\text{-}BMP\text{-}50}$ to $EL_{GBL\text{-}BMP\text{-}Cl\text{-}55}$ and from 28.6 to 19.7 Ah L^{-1} going from $EL_{MeCN\text{-}BMP\text{-}30}$ to $EL_{MeCN\text{-}BMP\text{-}Cl\text{-}30}$. Nevertheless, addition of [Cat]Cl seems to be necessary to reduce overpotentials, but [EMP]Cl and [BMP]Cl might be replaced by other additives inducing smoother deposition and stripping at lower cost of active mass/concentration. Additionally, an optimized membrane would improve the charge transport of chloride ions and allow for a reduction of the [Cat]Cl additive. An alternative solvent may further improve concentration. A last point, the variation of the cation in $[Cat]_2[Mn^{II}Cl_4]$ offers an opportunity to increase concentrations.

A high cell voltage (E_{cell}) is also necessary for a good energy density (cf. Equation (S1) Supporting Information). Unfortunately, a theoretical cell potential, which is often used for the calculation of the energy densities, is not accessible from the CV in GBL due to the high overpotential of the deposition reaction and the absence of the manganese stripping. However, in MeCN a cell potential of 2.48 V was estimated from the CV in Figure S16 (Supporting Information), in which all relevant electrochemical processes were observed, albeit with the overpotentials such that the true cell potential could be even higher. In addition, the open circuit potential (OCV) of a charged cell with $EL_{MeCN\text{-}BMP\text{-}Cl\text{-}30}$ was measured fifteen minutes after the battery was charged to SoC80 (Figure S32, Supporting Information) displayed an OCV of 2.42 V – in pleasing agreement with the CV experiment. For the $EL_{GBL\text{-}BMP\text{-}Cl\text{-}55}/EL_{GBL\text{-}BMP\text{-}Cl\text{-}55}$* cell, the same measurement yielded an increased OCV of 2.59 V. Since the theoretical cell potential in aqueous solution with Mn^{II}/Mn^{III} and Mn^0/Mn^{II} redox couples is 2.69 V, we assume that 2.59 V as measured here is a very reasonable lower limit (SoC80[64]) for E_{cell}. So far, the best all-MFB battery with respect to the number of realized cycles used $EL_{GBL\text{-}BMP\text{-}Cl\text{-}55}/EL_{GBL\text{-}BMP\text{-}Cl\text{-}55}$*. The energy density of this electrolyte is 27.8 Wh L^{-1}, which is, compared to new, state of the art VRFBs that have up to 40 Wh L^{-1}, quite unspectacular.[65,66] Given the fact that the investigation of VRFBs has been going on for several decades now, the energy density we realized already is quite impressive. Moreover, the $[EMP]^+$ based electrolyte $EL_{GBL\text{-}EMP\text{-}Cl\text{-}58}$ (46.3 Wh L^{-1}) already exceeds the energy density of the VRFB, with the potential to reach 64.8 Wh L^{-1} by reducing the amount of the [Cat]Cl additive. The highest energy density of 74.0 Wh L^{-1} observed was found for $EL_{MeCN\text{-}BMP\text{-}30}$ with MeCN as a solvent (Table 2).

2.5. Investigations in a Pumped Flow-Cell

Figure 11 shows the single cell setup used for the investigations in a pumped flow-cell, despite the battery casing would allow a series connection of up to three cells. The short distance between the electrodes necessitates the utilization of graphite felt electrodes (GFA6, from SGL Carbon), otherwise the membrane and the TF6 bipolar plate come into contact due the deflection of the membrane caused by small differential pressure in both half-cells. TF6 was used as electrode material for the positive and the negative electrode, since a solid manganese plate in the required size would be too brittle and expensive. The temperature of the flow-cell can be kept at a constant level, using heating foil placed behind the current collectors. The atmosphere in the battery cell, as well as the tubing was kept inert with a vacuum pump and an argon port that can be used alternatingly. The electrolyte was transferred to the tanks in an argon filled glovebox, which was coupled to the rest of the system under inert conditions. All components – the battery cell, the pump, the electrolyte tanks and the entire tubing – were placed in a specially designed box, in which the temperature was kept constant during the measurements using a heat exchanger. Additionally, to keep the atmosphere inert, a constant flow of nitrogen was passed through the box. Since we observed that the filling level of the catholyte tank decreased during cycling, accompanied by an increased filling level of the anolyte tank, a third tank with pure solvent was introduced into the system that allowed to adjust the filling level of the catholyte tank under inert conditions. After using a concentrated electrolyte in the first experiment, we decided to use diluted electrolytes afterward, since the amount of $[Cat]_2[Mn^{II}Cl_4]$ needed, is very high. A more detailed description of the Flow-cell setup can be found in the Supporting Information (Figures S33, S34, and S35, Supporting Information). All electrolytes used in the flow-cell are summarized in **Table 3**.

© 2021 The Authors. Advanced Energy Materials published by Wiley-VCH GmbH

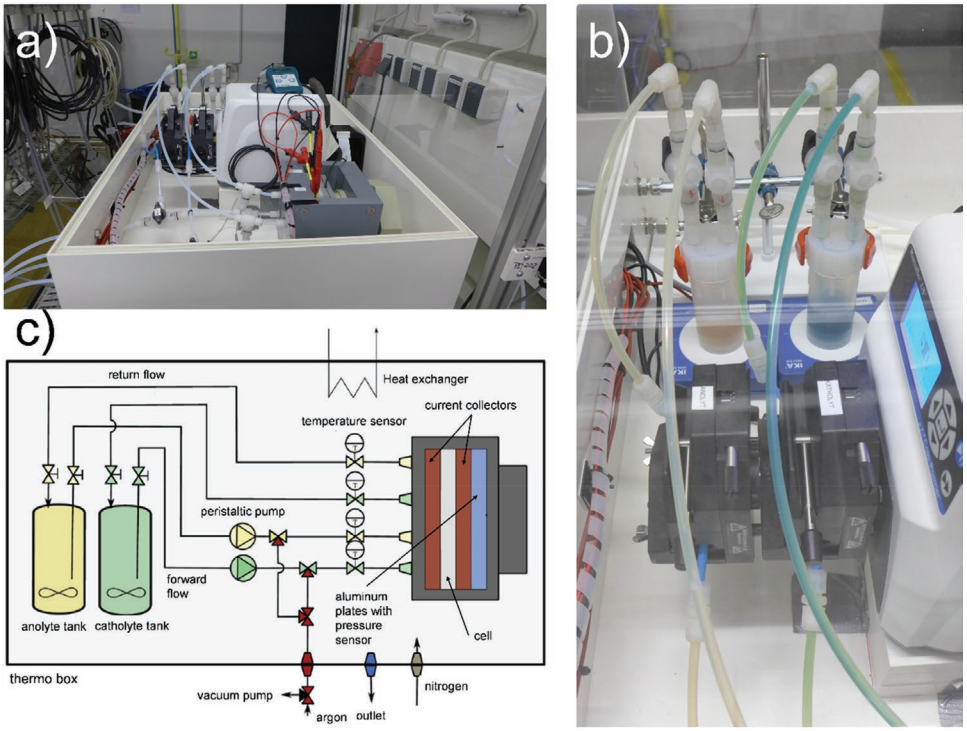

Figure 11. a) Setup for the measurements in a pumped flow-cell. b) Electrolyte tanks and tubing that display the characteristic colors of $[Mn^{II}Cl_4]^{2-}$ and $[Mn^{III}Cl_5]^{2-}$. c) Schematic view of the entire setup.

2.5.1. MeCN Based Electrolytes

MeCN had a series of negative effects on the materials, used for assembling the flow-cell, such as distorting PVDF frames and evaporating from the system during the experiment (see Figure S37, Supporting Information). Therefore, it was not possible to conduct a long-term cycling experiment with a MeCN based electrolyte. Nevertheless, we investigated the area specific resistance (ASR) and the cell potential (E_{cell}). The respective electrolytes, only differed in the Mn^{II} concentration (see Table 3). **Figure 12**a shows OCV measurements at SoC50 under various conditions. A stable voltage (U_{cell}) between 2.54 and 2.48 V was established for 69 h in the constantly pumped stack without felt electrodes with $EL_{MeCN\text{-}BMP\text{-}1.4}$ (blue line). This measurement, supports our estimations of E_{cell} of the all-MFB (CV: 2.48 V; OCV static cell: 2.42 V). After the measurement with a constant electrolyte flow, the pumps were stopped (orange line), showing that U_{cell} drops due to leaching immediately. A similar voltage drop appears, when the OCV of a static cell is measured in a charged state (see Figure S32, Supporting Information). In another experiment with low viscosity $EL_{MeCN\text{-}BMP\text{-}0.24}$ and felt electrodes a strong drop of U_{cell} was observed immediately after we stopped charging at SoC50, even though the electrolyte was pumped through the cell. Leaching seems to be enhanced through the felt electrodes, probably because $[Mn^{III}Cl_5]^{2-}$ is formed directly at the membrane. Although $EL_{MeCN\text{-}BMP\text{-}0.24}$ is diluted compared to $EL_{MeCN\text{-}BMP\text{-}1.4}$, we believe that the enhanced leaching can be assigned mainly to the utilization of the felt electrodes. This shows, that an optimized membrane is essential for the all-MFB because otherwise the round-trip efficiency suffers extremely. Figure 12b shows the ASR, determined at different temperatures, flow rates and with/without felt electrodes. The measurements with $EL_{MeCN\text{-}BMP\text{-}1.4}$ and different flow-rates showed a trend toward lower ASR-values at higher flow rates further reducing in going from 30°C to 40°C. A huge reduction of the ASR was observed with a diluted electrolyte and felt electrodes. Additionally, the ASR for charging and discharging the battery is at the same level if using felt electrodes. Without, the ASR for discharging was

Table 3. Abbreviations for the MeCN and GBL based electrolytes used in the flow-cell plus key parameters.

Electrolyte abbreviation	$[Cat]_2[Mn^{II}Cl_4]$	[Cat]Cl	$[Cat]_2[MnCl_4]$:[Cat]Cl (molar ratio)	Capacity[b]/Ah L^{-1}	c ($[Mn^{II}Cl_4]^{2-}$)/mol L^{-1}
$EL_{MeCN\text{-}BMP\text{-}1.4}$	$[BMP]_2[Mn^{II}Cl_4]$	–	–	18.76	1.40
$EL_{MeCN\text{-}BMP\text{-}0.24}$	$[BMP]_2[Mn^{II}Cl_4]$	–	–	3.22	0.24
$EL_{GBL\text{-}BMP\text{-}0.33\text{-}F}$[a]	$[BMP]_2[MnCl_4]$	–	–	4.39	0.33
$EL_{GBL\text{-}EMP\text{-}Cl\text{-}0.33\text{-}F/S}$[a]	$[EMP]_2[MnCl_4]$	[EMP]Cl	1:1	4.39	0.33

[a]The superscript -S or -F indicates, whether the measurements were performed in a static (-S) or a flow-cell (-F); [b]The volumetric capacity refers to the whole system (catholyte plus anolyte) and was calculated without the consideration of a two-electron process for the anolyte.

© 2021 The Authors. Advanced Energy Materials published by Wiley-VCH GmbH

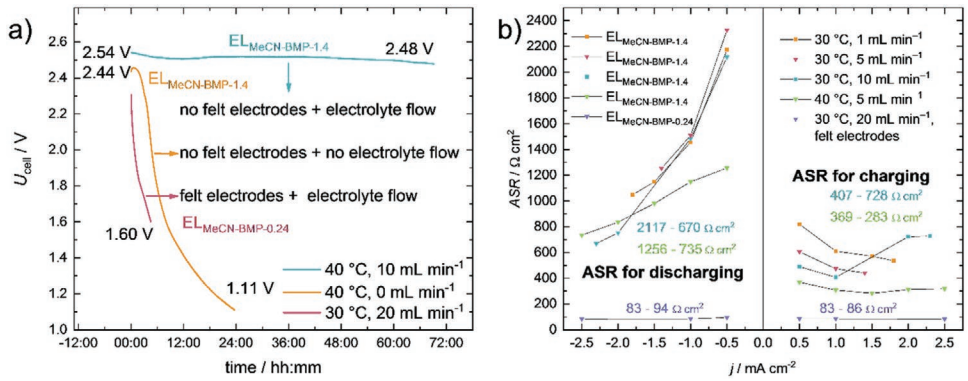

Figure 12. a) OCV measurements at SoC50. b) ASR measurements at SoC50.

significantly higher than for charging. Even with felt electrodes and a diluted electrolyte the ASR (82.6–94.4 Ω cm^2) is very high. Since it was established that an ASR < 5 Ω cm^2 is necessary for non-aqueous RFBs to be economically feasible,[67,68] the all-MFB is still far away from this requirement.

2.5.2. GBL Based Electrolytes

In contrast to the MeCN based electrolytes, two long-term cycling experiments with GBL based electrolytes were performed. Table 3 includes the key parameters of the two different electrolytes tested in the flow-cell. From $EL_{GBL\text{-}BMP\text{-}0.33}$ to $EL_{GBL\text{-}EMP\text{-}Cl\text{-}0.33}$ two essential modifications were made: The cation was changed from $[BMP]^+$ to $[EMP]^+$ in $[Cat]_2[MnCl_4]$ and additionally, [EMP]Cl was added as additive. With $EL_{GBL\text{-}EMP\text{-}Cl\text{-}0.33}$, 500 cycles over a period of two months were recorded. Table S20 (Supporting Information) shows the protocol used for the characterization of the electrolytes in a flow-cell. $EL_{GBL\text{-}EMP\text{-}Cl\text{-}0.33}$ was additionally tested in a static cell to evaluate the differences. **Figure 13** shows the corresponding results. Charging galvanostatically to SoC50 was not possible with $EL_{GBL\text{-}BMP\text{-}0.33\text{-}F}$, because the upper cutoff

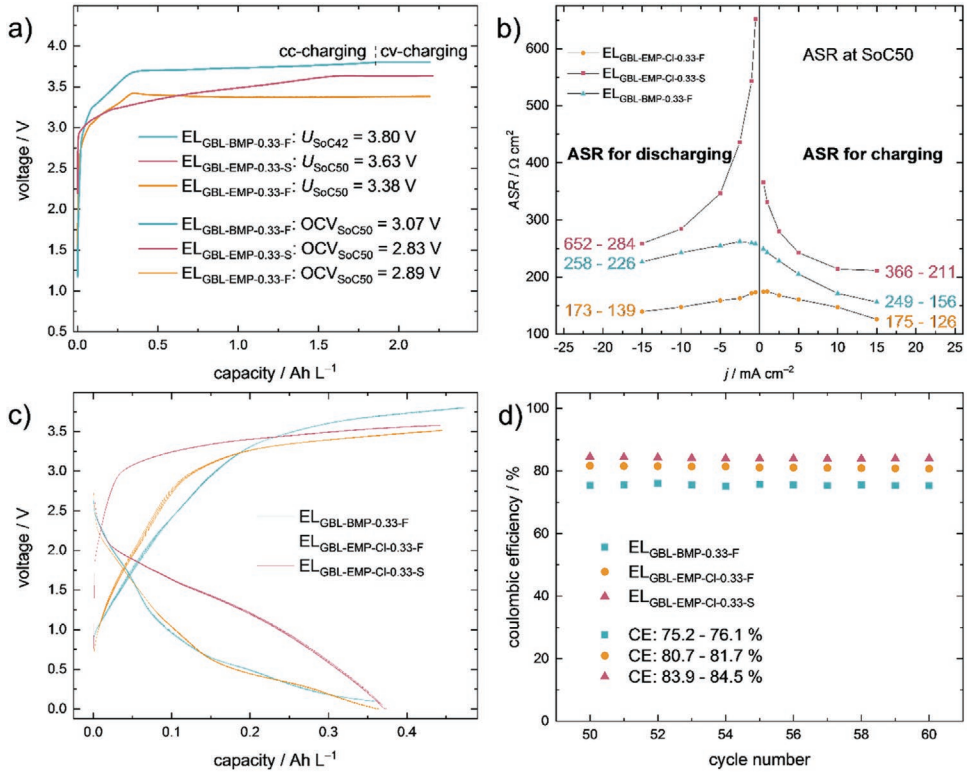

Figure 13. a) Voltage profiles of charging to SoC50 in a flow-cell with $EL_{GBL\text{-}BMP\text{-}0.33\text{-}F}$ and $EL_{GBL\text{-}EMP\text{-}Cl\text{-}0.33\text{-}F}$ and with $EL_{GBL\text{-}EMP\text{-}Cl\text{-}0.33\text{-}S}$ in a static cell. The current density was 1 mA cm^{-2} for each experiment. b) ASR at SoC50 for $EL_{GBL\text{-}BMP\text{-}0.33\text{-}F}$, $EL_{GBL\text{-}EMP\text{-}Cl\text{-}0.33\text{-}F}$ and $EL_{GBL\text{-}EMP\text{-}Cl\text{-}0.33\text{-}S}$. c) Voltage profiles of the cycles 50–60 of a cycling experiment, using 10%/11% of the capacity and a current density of 1.5 mA cm^{-2}. d) Corresponding coulombic efficiencies. For all experiments in the flow-cell a flow rate of 5 mL min^{-1} was used. The temperature for each experiment was 30 °C.

© 2021 The Authors. Advanced Energy Materials published by Wiley-VCH GmbH

voltage (3.8 V) was reached at SoC42. To reach SoC50 the cell was further charged with a constant voltage of 3.8 V. The higher charging voltage, needed for $EL_{GBL\text{-}BMP\text{-}0.33\text{-}F}$ without extra [Cat]Cl compared to $EL_{GBL\text{-}EMP\text{-}Cl\text{-}0.33\text{-}F}$ is caused by the higher ASR at SoC50 for the applied current density (Figure 13b).

By contrast, using $EL_{GBL\text{-}EMP\text{-}Cl\text{-}0.33\text{-}F}$ with extra chloride resulted in a desired stable voltage plateau around 3.38 V (U_{SoC50}). This shows the improvements resulting from the utilization of $[EMP]^+$ instead of $[BMP]^+$ and the addition of [EMP]Cl, with $EL_{GBL\text{-}EMP\text{-}Cl\text{-}0.33\text{-}F}$ having a lower ASR at all current densities compared to $EL_{GBL\text{-}BMP\text{-}0.33\text{-}F}$. The ASR of $EL_{GBL\text{-}EMP\text{-}Cl\text{-}0.33\text{-}S}$ (static cell) at SoC50 is higher at all current densities, compared to both electrolytes tested in the pumped flow-cell, probably due to the utilization of felt electrodes in the flow-cell (v.i.) absent in the static cell. As a result, the stable voltage plateau using $EL_{GBL\text{-}EMP\text{-}Cl\text{-}0.33\text{-}S}$ is established later compared to $EL_{GBL\text{-}EMP\text{-}Cl\text{-}0.33\text{-}F}$ and also higher by 0.25 V, lying around 3.63 V (U_{Soc50}). Figure 13c shows the voltage profiles of the cycles 50–60 of the cycling experiments. The charge voltages (U_{SoC10}) follow the same order observed for U_{SoC50}. Favorably, while the voltages during discharge for $EL_{GBL\text{-}EMP\text{-}Cl\text{-}0.33\text{-}F}$ and $EL_{GBL\text{-}BMP\text{-}0.33\text{-}F}$ (flow-cell) are very similar, the voltage of $EL_{GBL\text{-}EMP\text{-}Cl\text{-}0.33\text{-}S}$ (static cell) is clearly higher. This is surprising, given the ASR for discharging is significantly higher for $EL_{GBL\text{-}EMP\text{-}Cl\text{-}0.33\text{-}S}$ compared to $EL_{GBL\text{-}BMP\text{-}0.33\text{-}F}$ and $EL_{GBL\text{-}EMP\text{-}Cl\text{-}0.33\text{-}F}$. Again, the utilization of felt electrodes in the pumped cell might be the reason for this. In the static cell, without the felt electrodes, the electrochemical reactions are spatially separated from the membrane. In the flow-cell, while charging, $[Mn^{III}Cl_5]^{2-}$ is formed directly at the membrane. This leads to a drastically decreased distance that has to be traveled by diffusion, for passing the membrane, which is probably accelerated further by the constant electrolyte flow in the flow-cell. Therefore, through leaching, $[Mn^{III}Cl_5]^{2-}$ enters the negative half-cell much faster in the flow-cell and can influence the voltage while discharging. This goes along very well with the observations made with $EL_{MeCN\text{-}BMP\text{-}0.24}$, where the introduction of felt electrodes also enhanced leaching. The assumption is further supported by the CE, which is 3% higher for $EL_{GBL\text{-}EMP\text{-}Cl\text{-}0.33\text{-}S}$ compared to $EL_{GBL\text{-}EMP\text{-}Cl\text{-}0.33\text{-}F}$. The higher CE in the static cell results from the reduced leaching. The 5% lower CE of $EL_{GBL\text{-}BMP\text{-}0.33\text{-}F}$ compared to $EL_{GBL\text{-}EMP\text{-}Cl\text{-}0.33\text{-}F}$ is probably caused by the higher ASR of $EL_{GBL\text{-}BMP\text{-}0.33\text{-}F}$. Thus, the lower cutoff voltage (0 V) is reached before the battery is discharged completely. During the experiments in the flow-cell, a decrease of the filling level in the catholyte tank (Mn^{II}/Mn^{III} half-cell) was observed, accompanied by an increase of the filling level in the anolyte tank (Mn^{II}/Mn^0 half-cell), for both, $EL_{GBL\text{-}BMP\text{-}0.33\text{-}F}$ and $EL_{GBL\text{-}EMP\text{-}Cl\text{-}0.33\text{-}F}$. This phenomenon cannot be observed in a static cell, even if it takes place. The reason for the change in the filling levels is probably osmotic pressure, caused by an increasing number of ions in the anolyte while charging. For each manganese atom that is deposited, four chloride ions are released. On the other hand, the number of ions in the catholyte remains constant, since the chloride ions that pass the membrane for charge balancing react with $[Mn^{II}Cl_4]^{2-}$ to form $[Mn^{III}Cl_5]^{2-}$ upon oxidation. To continue cycling the battery, pure solvent was introduced to the system by a refill of the catholyte tank under inert conditions. For $EL_{GBL\text{-}BMP\text{-}0.33\text{-}F}$ this refill was necessary after 66 cycles, whereas for $EL_{GBL\text{-}EMP\text{-}Cl\text{-}0.33\text{-}F}$ the refill took place after cycle 207 (see **Figure 14**d), showing an improved cycling stability. Hence, the introduction of additional [Cat]Cl already improved this problem and gives hope that it can be overcome completely by adding optimized amounts of [Cat]Cl to the anolyte and the catholyte. Thus, $EL_{GBL\text{-}EMP\text{-}Cl\text{-}0.33}$ is superior to $EL_{GBL\text{-}BMP\text{-}0.33}$ concerning the ASR, the CE, and the cycling stability. Whether the different cation or the addition of [Cat]Cl has the larger impact cannot be distinguished, but we assume that both modifications have a significant participation.

2.5.3. Long Term Cycling

Figure 14 shows the results of the entire cycling experiment (500 cycles) with $EL_{GBL\text{-}EMP\text{-}Cl\text{-}0.33\text{-}F}$ with a refill of the catholyte tank with pure GBL after 207 cycles at 30°C. During these cycles the CE was between 61% and 83%, decreasing from 76% to 74% during the last 50 cycles before the GBL refill. During the following 13 cycles at 30 °C the CE was at 76% again. At 40 °C the CE dropped to 58%, probably caused by the increased mobility of $[Mn^{II}Cl_5]^{2-}$, resulting in an enhanced leaching. Back at 30 °C, the CE stabilized around 70% again. At 50 °C, the CE dropped even further to 21%, but started to increase after the temperature was set back to 30 °C after 18 cycles. When the capacity utilization (C_U) started to fade after 333 cycles from 10% to 2% over the next 170 cycles, the CE was again at 30%. At the end of the last 170 cycles the CE reached 75% again. Although the battery was cycled in a range of only 10% of the entire capacity, the number of cycles, before the capacity started to fade shows that the principle of using $[Mn^{II}Cl_4]^{2-}$ as active material in both half cells, to achieve a long lifetime of the battery, works. The ability to regenerate the CE after increased temperatures shows additionally that the system can tolerate harsh conditions. Figure 14e) shows the development of the ASR over the time of the whole experiment. During the first 207 cycles at 30 °C, the ASR increased, which is probably the reason for the slowly decreasing CE (83–74%). Refilling the catholyte tank with GBL did not influence the ASR. At 40 °C, the ASR is at its minimum during the entire experiment. However, the enhanced leaching prevents an improvement of the CE through the lower ASR. At 50 °C the ASR rises again, especially upon discharging. Afterwards at 30 °C the ASR is at its maximum. Figure 14c) shows a photograph of the membrane after the cycling experiment. A strong alteration of the originally white membrane surface to black/brown can be observed. It is therefore possible that the pores of the membrane became blocked by particles over the course of the experiment. This might explain the constantly rising ASR during the cycling and is probably also the reason for the decreasing capacity, starting after cycle 333. The TF6 material at the negative electrode showed the same type of alteration, observed during the measurements in the static cells, which might have an influence on the ASR as well.

Table 4 shows a comparison of the ASR with different electrolytes. Using $[EMP]^+$ and additional [Cat]Cl in $EL_{GBL\text{-}EMP\text{-}Cl\text{-}0.33\text{-}F}$ compared to $EL_{GBL\text{-}BMP\text{-}0.33\text{-}F}$ resulted in a significant decrease of the ASR. Still, the ASR with $EL_{GBL\text{-}EMP\text{-}Cl\text{-}0.33\text{-}F}$ is significantly higher compared to the ASR of $EL_{MeCN\text{-}BMP\text{-}0.24}$, although $[BMP]^+$ was used as a cation and no additional [Cat]Cl was added.

© 2021 The Authors. Advanced Energy Materials published by Wiley-VCH GmbH

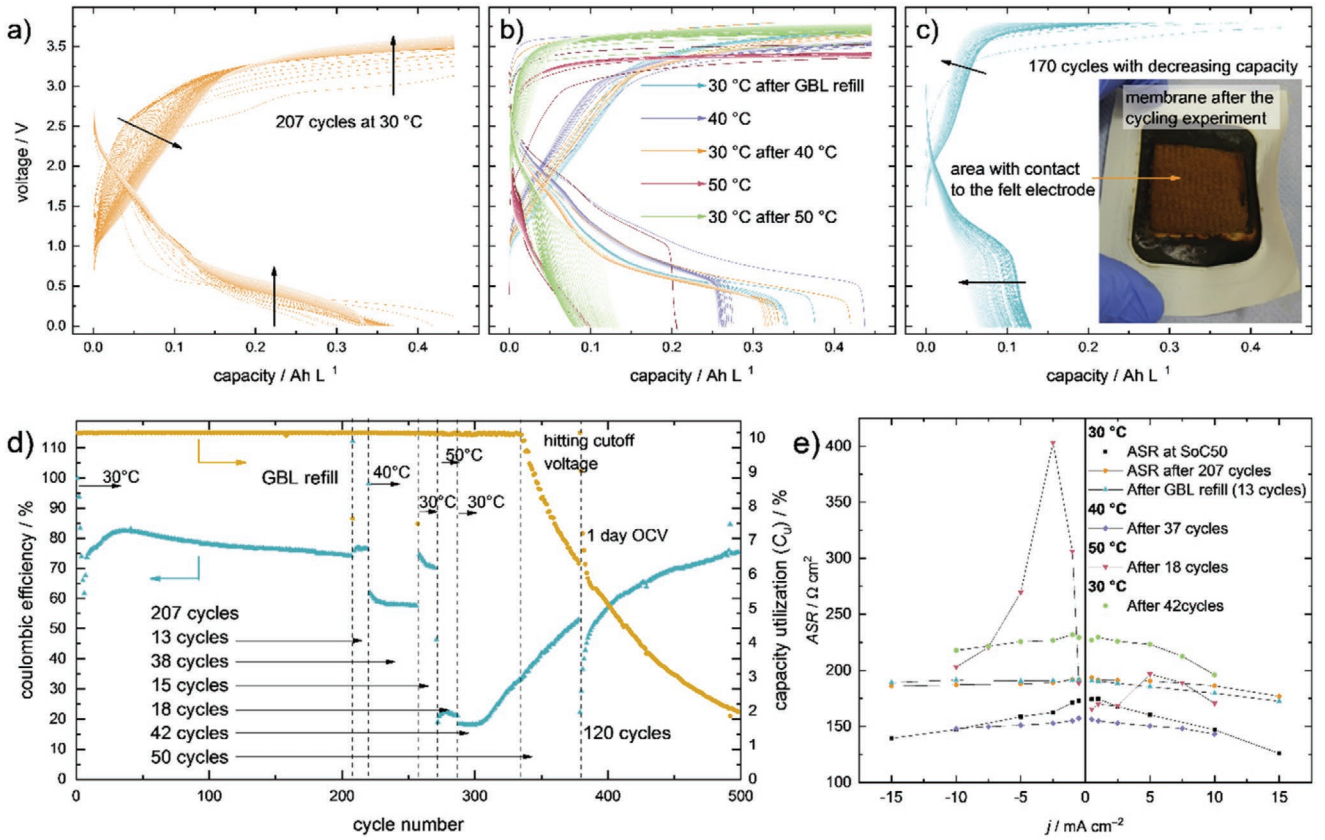

Figure 14. Voltage profiles with $EL_{GBL\text{-}EMP\text{-}Cl\text{-}0.33\text{-}F}$ using a current density of 1.5 mA cm^{-2}, a flow rate of 5 mL min^{-1} and a temperature of 30 °C. a) Cycles 1–207 b) cycles 208–333 c) cycles 331 to 500, while the capacity utilization (C_U) fades plus photograph of the membrane after the cycling experiment. d) Overview of the entire cycling experiment with $EL_{GBL\text{-}EMP\text{-}Cl\text{-}0.33\text{-}F}$ using a current density of 1.5 mA cm^{-2}, a flow rate of 5 mL min^{-1}. e) ASR measured at different moments during the cycling experiment.

2.6. Processes that Influence the Performance of the All-MFB

Figure 15 shows a comparison of the pumped flow-cell and a static battery cell using $EL_{GBL\text{-}EMP\text{-}Cl\text{-}0.33}$, TF6 as electrode material at the positive and the negative electrode and the FAPQ-375-PP membrane. Graphite felt electrodes were used additionally in the flow-cell (v.s.), whereas only the planar TF6 electrode material was used in the static battery cell. Figure 15a,b show the CE and the C_u of the two cells. Since a temperature control is not possible in the static cells, the measurement took place at ≈30 °C, whereas a temperature variation was conducted with the flow-cell (v.s.).

In both experiments the CE rises at the beginning, reaching a maximum after 14 cycles in the static cell and 41 cycles in the pumped flow-cell with CEs of 85.5% and 83.2%, respectively. After this maximum, the CE decreases slowly, reaching 79.0% (static) and 74.5% (pumped) after 200 cycles. In the flow-cell a GBL refill for the catholyte tank was necessary after cycle 207, and after cycle 220 the temperature variation started, which had a huge impact on the CE (see Figure 15b). Therefore, it is not possible to compare the CE any further after cycle 200. In the static cell however, the CE continues to decrease slowly ending at 74.2% at cycle 500. In the pumped flow-cell, the CE is slightly lower compared to the static cell (74.5–83.2% vs 79.0–85.5%). We explain this difference with the utilization of felt electrodes in the flow-cell. Due to the felt electrodes, the active species are generated directly next to the membrane, with the consequence that the distance that has to be travelled for leaching is drastically reduced. The enhanced leaching in the pumped flow-cell, caused by felt electrodes, is further supported by the observation of a strong drop in U_{cell} (Figure 12a, red line). Without felt electrodes, a stable U_{cell} can be observed for 69 h (Figure 12a, blue line). Apart from this difference, the behavior of the CE is in great accordance between the static cell and the

Table 4. Comparison of the ASR at SoC50 for different electrolytes in the flow-cell.

	ASR at SoC50 for charging/Ω cm^2	ASR at SoC50 for discharging/Ω cm^2	Solvent	[Cat]$^+$	Add. [Cat]Cl
$EL_{GBL\text{-}BMP\text{-}0.33\text{-}F}$	156–249	226–258	GBL	[BMP]$^+$	no
$EL_{GBL\text{-}EMP\text{-}Cl\text{-}0.33\text{-}F}$	126–175	139–173	GBL	[EMP]$^+$	yes
$EL_{MeCN\text{-}BMP\text{-}0.24}$	83–86	83–94	MeCN	[BMP]$^+$	no

© 2021 The Authors. Advanced Energy Materials published by Wiley-VCH GmbH

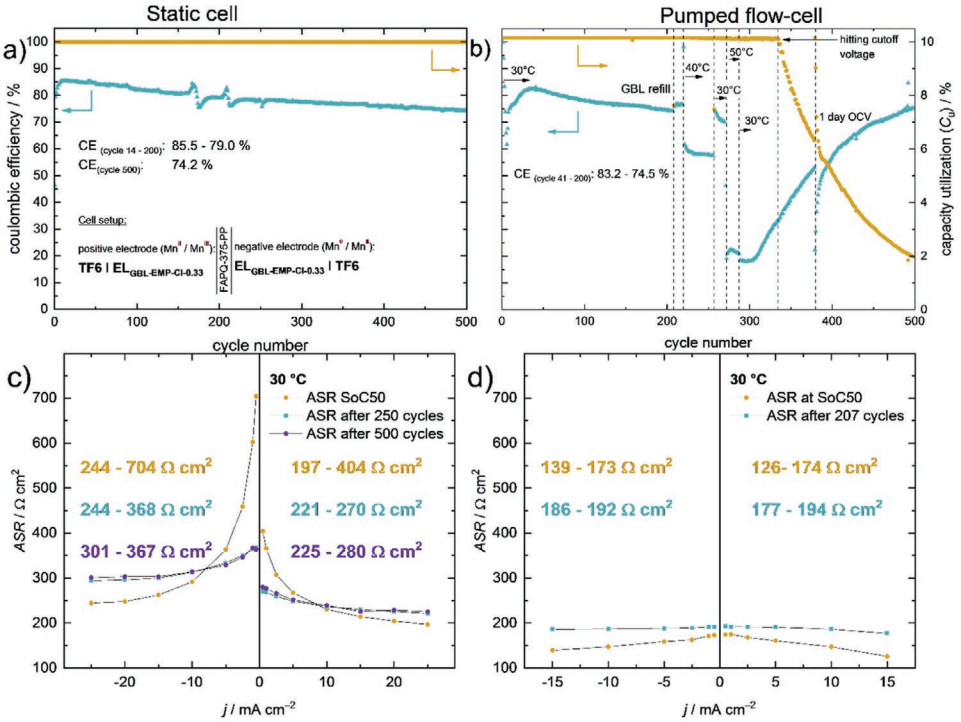

Figure 15. a) CE and C_u of a static battery cell with $EL_{GBL-EMP-Cl-0.33}$ over 500 cycles using a current density of 1.5 mA cm^{-2} at 30 °C. b) CE and C_u of a pumped flow-cell with $EL_{GBL-EMP-Cl-0.33}$ over 500 cycles using a current density of 1.5 mA cm^{-2} at different temperatures. c) ASR of a static battery cell with $EL_{GBL-EMP-Cl-0.33}$ at different moments during the cycling experiment. d) ASR of a pumped flow-cell with $EL_{GBL-EMP-Cl-0.33}$ at different moments during the cycling experiment.

pumped flow-cell. Nevertheless, CEs between 74.2% and 85.5% (static cell) are not satisfying, and have to be further improved. Although in a pumped setup, leaching is reduced to the electrolyte in the cell, when the pumps do not work (v.s.), it has to be reduced as much as possible to improve the overall efficiency.

2.7. Potential for Further CE-Optimization

During this work, the following parameters were identified having an impact on the CE: the membrane, the ASR and the Mn deposition.

2.7.1. Membrane

The impact, of different membranes on the CE is shown in Figure S13 (Supporting Information). A membrane that cannot prevent the leaching of $[Mn^{III}Cl_5]^{2-}$ into the negative half-cell contributes to a reduced CE, because the desired cell reactions occur chemically instead of electrochemically. Yet, the AEM FAPQ-375-PP is prone to leaching, but was the best alternative, we had at our disposal and with changing from FAPQ-310 (CE = 49.9%) to FAPQ-375-PP (CE = 88.4%) the CE already improved by 38.5%. Without any membrane, the CE was around 14.4%. The reduction of the CE between the SoC5 and the SoC80 cycling experiments (70% vs 35%) also shows the strong effect of leaching on the CE. With a membrane especially designed for the all-MFB, the CE could therefore be improved drastically.

2.7.2. ASR

Not only the CE, but also the C_u, can be improved with a reduction of the ASR. Figure 15c,d shows the ASR for the static, as well as the pumped flow-cell at different moments during the cycling experiment. In general, the ASR of the static cell is much higher compared to the ASR in the flow-cell, due to the utilization of felt electrodes and a constant electrolyte flow in the pumped flow-cell. Many parameters influence the ASR and we do not claim to cover all effects, but at least the ones we observed during this work. Table 4 shows, that the addition of [Cat]Cl, as well as the solvent have a huge impact on the ASR. With a MeCN based electrolyte ($EL_{MeCN-BMP-0.24}$), values between 83 and 94 Ω cm^2 were measured. Although the respective electrolyte did not contain extra [Cat]Cl, the ASR is already lower compared to a GBL based electrolyte with add. [Cat]Cl ($EL_{GBL-EMP-Cl-0.33}$; ASR = 126–175 Ω cm^2). The reason, appears to be the higher conductivity and lower viscosity of MeCN based electrolytes compared to GBL based electrolytes (cf. Table 1). Continuing the search for electrochemically stable solvents that show a good solubility of $[Cat]_2[Mn^{II}Cl_4]$, high conductivity and low viscosity, might be very rewarding. With a high ASR the CE is lower and the discharge of the battery is not complete, because the lower cut-off voltage is hit, before the battery is discharged completely. Often, a green catholyte ($[Mn^{III}Cl_5]^{2-}$) was withdrawn from the presumably discharged battery cells. Thus, a reduction of the ASR will improve the CE. The following parameters can also influence the ASR: the membrane, electrode materials, pre-treatment of the electrode materials, improved kinetics of the electrochemical reactions and the flow geometry.

© 2021 The Authors. Advanced Energy Materials published by Wiley-VCH GmbH

2.7.3. Manganese Deposition

Experiments concerning the deposition of manganese (Figures 3, 4, and 6) showed that a mechanically unstable Mn layer is formed when the battery is charged. Manganese does not stick to the electrode ("dead" manganese). Therefore, it cannot be stripped during discharge, which leads to a reduction of the CE. However, the complexity of metal deposition is high and many parameters like temperature, current density, additives and more exist to influence these processes, maybe leading to a dense and stable Mn layer.[69] Yet, before that, a better suited electrode material has to be found. We already showed in this work, that TF6 is sub-optimal, since it is not electrochemically inert at the negative potential necessary for Mn deposition (Figure S30, Supporting Information). Still, many different types of graphite exist and a suitable variant for the deposition of Mn may become available. Since the LSV experiment (Figure S12, Supporting Information) suggests only limited passivation of the electrode surface during the anodic dissolution of Mn^0, we believe that the high overpotential of 0.85 to 0.87 V (see Figure 6), results mainly from the deposition of manganese, potentially due to its unusual elemental structure. The unfavorable electrochemical reduction of Mn^{II} as the dianion $[Mn^{II}Cl_4]^{2-}$, i.e., Coulomb repulsion at the negatively charged electrode, might be a reason for that. It could be overcome with the utilization of additives. Together with the other parameters, mentioned earlier, the high overpotential, which is much too high for technical application, could be reduced reaching acceptable energy efficiencies and higher CEs.

Despite a CE between 74.2% and 85.5% (static cell), we believe that the all-MFB is a very promising system. Approaching the key problems, discussed in this paragraph, we think that the performance of the all-MFB has the potential to be pushed to a level, where it becomes a serious competitor for EES.

3. Conclusion

In this work we investigated the feasibility of $[Cat]_2[Mn^{II}Cl_4]$ as an active material for the positive and the negative electrode of a hybrid-RFB, showing on a first principle level that the intended all-MFB works in a pumped flow-cell. **Figure 16** shows a schematic representation of the cell reactions, namely the oxidation of $[Mn^{II}Cl_4]^{2-}$ to $[Mn^{III}Cl_5]^{2-}$ at the positive electrode and Mn^0 deposition from $[Mn^{II}Cl_4]^{2-}$ at the negative electrode. Using different methods, including cyclic voltammetry, linear sweep voltammetry and symmetric half-cell experiments we showed that these reactions are electrochemically reversible in MeCN and GBL.

Using these solvents, electrolytes were developed for a systematic study in static battery cells, before testing the most promising electrolytes in an actual pumped flow-cell. Using temperature dependent viscosity and conductivity measurements, we showed that the performances of the electrolytes are comparable to electrolytes used in LIBs. According to Walden plots, derived from these measurements, an acceptable ionicity was observed, leaving room for further improvements. In the battery, the main problems, we identified are the formation of a mechanically unstable Mn film, a high overpotential (≈0.88 V) for the

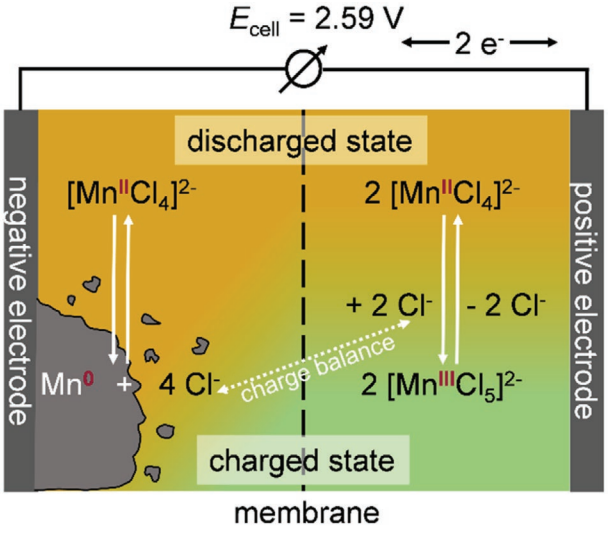

Figure 16. Schematic representation of the electrochemical processes taking place in the all-Mn battery, also showing the problems, namely leaching and Mn deposition.

deposition of manganese and the leaching of $[Mn^{II}Cl_5]^{2-}$ toward the negative electrode. Capacity fading, due to "dead" manganese, a low energy efficiency and a reduced CE (74.2–85.5% in a static cell) result. The mechanically unstable Mn film is caused by a cauliflower like deposition of manganese, shown with SEM measurements. However, for the formation of a mechanically stable Mn film and the reduction of the overpotential a broad variety of parameters can be optimized, such as the utilization of additives, alternative electrode materials, different pretreatments of the electrode materials, other solvents, conditioning cycles and so on. The leaching problem may be overcome with an optimized membrane, preventing $[Mn^{III}Cl_5]^{2-}$ from passing, but allowing chloride ions to do so. With an electrolyte based on $[EMP]_2[Mn^{II}Cl_4]$ energy densities up to 64.8 Wh L^{-1} are possible in GBL, whereas 74 Wh L^{-1} can be reached with a $[BMP]_2[Mn^{II}Cl_4]$ electrolyte in MeCN. A cell potential (E_{cell}) of 2.59 V and concentrations of up to 1.6 mol L^{-1} enable these energy densities. The straight forward synthesis of $[Cat]_2[Mn^{II}Cl_4]$, which was conducted on a 200 g scale, allows a variation of the cation and even the introduction of two different cations. This might lead to improved solubility and therefore to even higher energy densities. At the positive electrode, we identified graphite materials as suitable, whereas at the negative electrode the graphite is not electrochemically inert any more at the applied potentials, which was shown with CV measurements using an electrochemically inert supporting electrolyte. Apparently, intercalation of $[Cat]^+$ takes place, next to the deposition of manganese. In a pumped flow-cell, an electrolyte based on $[EMP]_2[Mn^{II}Cl_4]$ and [EMP]Cl in GBL (0.33 mol L^{-1}) was cycled over two months, with CEs up to 83%, which is comparable to the CE, observed in the static cells. 333 cycles were recorded with a capacity utilization (C_U) of 10% as designated, followed by 170 cycles with a fading C_U. This shows, that the principle of using $[Mn^{II}Cl_4]^{2-}$ as active material in both half-cells works, to achieve a long cycle life. The capacity fading, during the last 170 cycles probably resulted from the increasing area specific resistance (ASR) during the cycling. Therefore, the

© 2021 The Authors. Advanced Energy Materials published by Wiley-VCH GmbH

upper cut-off voltage of 3.8 V was hit, before the battery could be charged to a C_U of 10%. It is possible that the electrolyte could be cycled further, but the ASR became too high for that. From this, and other experiments in the flow-cell, we learned that the ASR is too high in the all-MFB, already at the beginning of the cycling. With a MeCN based electrolyte an ASR between 83 and 94 Ω cm^2 was measured, which is still far away from 5 Ω cm^2, which has to be beaten for an economically feasible battery. However, a lot of parameters can be improved to further reduce the ASR. Since this is a first principle study, focusing on the question, whether an all-MFB is possible at all, we did not focus on the optimization of every parameter. The following parameters for reducing the ASR, starting with the most promising ones are: membrane/separator, electrode materials, pre-treatments of electrode materials, increased electrolyte conductivity and a mechanically stable manganese deposition. This lists the parameters, which are the most relevant ones in our opinion, but does not claim to be complete. Maybe other parameters like an optimized flow geometry might also have a huge impact. Compared to the benchmark VRFB system, the all-MFB has a higher energy density and is based on the cheap and abundant element manganese. Additionally, there is still a lot of room for improvements, making the all-MFB presented in this work an interesting field for further research.

Supporting Information

Supporting Information is available from the Wiley Online Library or from the author.

Acknowledgements

This work was supported by the Albert-Ludwigs-Universität of Freiburg, the FU Berlin and the BMBF in the project IL-RFB (FKZ 03SF0526A). A special thanks goes to Dr. Thilo Ludwig for measuring the pXRD and Anita Becherer for support in obtaining SEM-EDX measurements. The use of the SEM-EDX set up, acquired through the BMBF project EDELKAT (FKZ 03X5524), is gratefully acknowledged. The authors also thank Dr. Simon Steinhauer, Patrick Voßnacker and Thomas Keilhack from the FU Berlin as well as Dr. Valentin Radtke from Freiburg for helpful scientific discussions.

Open access funding enabled and organized by Projekt DEAL.

Conflict of Interest

The authors declare no conflict of interest.

Data Availability Statement

The data that support the findings of this study are available from the corresponding author upon reasonable request.

Keywords

anolytes, catholytes, manganese, non-aqueous, redox-flow batteries

Received: April 21, 2021
Published online: May 24, 2021

[1] P. Alotto, M. Guarnieri, F. Moro, *Renewable Sustainable Energy Rev.* **2014**, *29*, 325.
[2] E. Sánchez-Díez, E. Ventosa, M. Guarnieri, A. Trovò, C. Flox, R. Marcilla, F. Soavi, P. Mazur, E. Aranzabe, R. Ferret, *J. Power Sources* **2021**, *481*, 228804.
[3] Z. Yang, J. Zhang, M. C. W. Kintner-Meyer, X. Lu, D. Choi, J. P. Lemmon, J. Liu, *Chem. Rev.* **2011**, *111*, 3577.
[4] D. Larcher, J.-M. Tarascon, *Nat. Chem.* **2015**, *7*, 19.
[5] T. Kim, W. Song, D.-Y. Son, L. K. Ono, Y. Qi, *J. Mater. Chem. A* **2019**, *7*, 2942.
[6] X. Wei, W. Pan, W. Duan, A. Hollas, Z. Yang, B. Li, Z. Nie, J. Liu, D. Reed, W. Wang, V. Sprenkle, *ACS Energy Lett.* **2017**, *2*, 2187.
[7] Y. Liang, H. Dong, D. Aurbach, Y. Yao, *Nat. Energy* **2020**, *5*, 646.
[8] H. Chen, T. N. Cong, W. Yang, C. Tan, Y. Li, Y. Ding, *Prog. Nat. Sci.* **2009**, *19*, 291.
[9] Á. Cunha, J. Martins, N. Rodrigues, F. P. Brito, *Int. J. Energy Res.* **2015**, *39*, 889.
[10] Q. Huang, Q. Wang, *ChemPlusChem* **2015**, *80*, 312.
[11] R. Borah, F. R. Hughson, J. Johnston, T. Nann, *Mater. Today Chem.* **2020**, *6*, 100046.
[12] D. K. Walanda, G. A. Lawrance, S. W. Donne, *J. Power Sources* **2005**, *139*, 325.
[13] A. E. S. Sleightholme, A. A. Shinkle, Q. Liu, Y. Li, C. W. Monroe, L. T. Thompson, *J. Power Sources* **2011**, *196*, 5742.
[14] J. Lu, D. Dreisinger, T. Glück, *Hydrometallurgy* **2014**, *141*, 105.
[15] C. R. Groom, I. J. Bruno, M. P. Lightfoot, S. C. Ward, *Acta Crystallogr., Sect. B: Struct. Sci., Cryst. Eng. Mater.* **2016**, *72*, 171.
[16] P. C. Moews, *Inorg. Chem.* **1966**, *5*, 5.
[17] R. A. Lalancette, N. Elliott, I. Bernal, *J. Cryst. Mol. Struct.* **1972**, *2*, 143.
[18] G. Bergerhoff, I. D. Brown, *Crystallographic Databases*.
[19] R. J. H. Clark, T. M. Dunn, *J. Chem. Soc.* **1963**, 1198.
[20] H. G. M. Edwards, M. J. Ware, L. A. Woodward, *Chem. Commun.* **1968**, 540.
[21] H. G. M. Edwards, L. A. Woodward, M. J. Gall, M. J. Ware, *Spectrochim. Acta* **1970**, *26*, 287.
[22] S. Pitula, A.-V. Mudring, *Chem. – Eur. J.* **2010**, *16*, 3355.
[23] J.-C. Chang, W.-Y. Ho, I.-W. Sun, Y.-K. Chou, H.-H. Hsieh, T.-Y. Wu, *Polyhedron* **2011**, *30*, 497.
[24] F. A. Cotton, L. M. Daniels, P. Huang, *Inorg. Chem.* **2001**, *40*, 3576.
[25] H. Mashiyama, N. Koshiji, *Acta Crystallogr., Sect. B: Struct. Sci.* **1989**, *45*, 467.
[26] A. R. Parent, C. P. Landee, M. M. Turnbull, *Inorg. Chim. Acta* **2007**, *360*, 1943.
[27] N. S. Gill, R. S. Nyholm, *J. Chem. Soc.* **1959**, 3997.
[28] C. F. Bell, D. N. Waters, *J. Inorg. Nucl. Chem.* **1977**, *39*, 773.
[29] W. Levason, C. A. McAuliffe, *Dalton Trans.* **1973**.
[30] Y. Rojas, M. Tadrosse, C. Assaf, I. Bernal, R. A. Lalancette, *Struct. Chem.* **2020**, *31*, 1309.
[31] M. Matsui, S. Koda, S.'i. Ooi, H. Kuroya, I. Bernal, *Chem. Lett.* **1972**, *1*, 51.
[32] I. Bernal, N. Elliott, R. Lalancette, *J. Chem. Soc. D* **1971**, *0*, 803.
[33] S. Walha, H. Naili, S. Yahyaoui, B. F. Ali, M. M. Turnbull, T. Mhiri, T. Bataille, *Solid State Sci.* **2011**, *13*, 204.
[34] R. F. Weinland, P. Dinkelacker, *Z. Anorg. Chem.* **1908**, *60*, 173.
[35] J. Sniekers, J. C. Malaquias, L. van Meervelt, J. Fransaer, K. Binnemans, *Dalton Trans.* **2017**, *46*, 2497.
[36] J.-K. Chang, C.-H. Huang, W.-T. Tsai, M.-J. Deng, I.-W. Sun, P.-Y. Chen, *Electrochim. Acta* **2008**, *53*, 4447.
[37] S. Zein El Abedin, E. M. Moustafa, R. Hempelmann, H. Natter, F. Endres, *ChemPhysChem* **2006**, *7*, 1535.
[38] J. S. Avery, C. D. Burbridge, D. M. L. Goodgame, *Spectrochim. Acta* **1968**, *24*, 1721.
[39] F. A. Cotton, D. M. L. Goodgame, M. Goodgame, *J. Am. Chem. Soc.* **1962**, *84*, 167.

© 2021 The Authors. Advanced Energy Materials published by Wiley-VCH GmbH

[40] T. S. Davis, J. P. Fackler, M. J. Weeks, *Inorg. Chem.* **1968**, *7*, 1994.
[41] A. F. Holleman, E. Wiberg, N. Wiberg, *Lehrbuch der anorganischen Chemie*, de Gruyter, Berlin **2007**.
[42] A. M. Bond, E. A. McLennan, R. S. Stojanovic, F. G. Thomas, *Anal. Chem.* **1987**, *59*, 2853.
[43] W. D. Sides, Q. Huang, *Electrochim. Acta* **2018**, *266*, 185.
[44] Since we were mainly interested whether a deposition is possible, we did not focus on the exact potential and used a Pt-wire as a quasi-reference electrode, which is sufficient for such experiments.
[45] J. A. Oberteuffer, J. A. Ibers, *Acta Crystallogr., Sect. B: Struct. Sci.* **1970**, *26*, 1499.
[46] S. SASAKI, K. FUJINO, Y. TAKÉUCHI, *Proc. Jpn. Acad., Ser. B* **1979**, *55*, 43.
[47] A. P. Abbott, G. Frisch, J. Hartley, W. O. Karim, K. S. Ryder, *Prog. Nat. Sci.* **2015**, *25*, 595.
[48] D. R. Lide, in *CRC Handbook of Chemistry and Physics*, CRC Press, Boca Raton, FL **2007**, p. 2006.
[49] D. H. S. Ramkumar, A. P. Kudchadker, *J. Chem. Eng. Data* **1989**, *34*, 463.
[50] W. Beichel, P. Eiden, I. Krossing, *ChemPhysChem* **2013**, *14*, 3221.
[51] J. Kasnatscheew, R. W. Schmitz, R. Wagner, M. Winter, R. Schmitz, *J. Electrochem. Soc.* **2013**, *160*, A1369.
[52] R. W. Schmitz, P. Murmann, R. Schmitz, R. Müller, L. Krämer, J. Kasnatscheew, P. Isken, P. Niehoff, S. Nowak, G.-V. Röschenthaler, N. Ignatiev, P. Sartori, S. Passerini, M. Kunze, A. Lex-Balducci, C. Schreiner, I. Cekic-Laskovic, M. Winter, *Prog. Solid. State Chem.* **2014**, *42*, 65.
[53] N. Takami, T. Ohsaki, H. Hasebe, M. Yamamoto, *J. Electrochem. Soc.* **2002**, *149*, A9.
[54] D. R. MacFarlane, M. Forsyth, E. I. Izgorodina, A. P. Abbott, G. Annat, K. Fraser, *Phys. Chem. Chem. Phys.* **2009**, *11*, 4962.
[55] M. Schleep, S. Reininger, P. Eiden, P. Klose, C. Schulz, H. Scherer, S. Laule, S. Bodendorfer, M. Schmidt, A. Garsuch, I. Krossing, *ChemElectroChem* **2016**, *3*, 774.
[56] J. B. Goodenough, Y. Kim, *Chem. Mater.* **2010**, *22*, 587.
[57] Therefore, it is possible that migration of the electrochemically active species is not eliminated during the measurement. Strictly, it is therefore not possible to apply the common diagnostic criteria to evaluate the reversibility of the $[Mn^{II}Cl_4]^{2-}/[Mn^{III}Cl_5]^{2-}$ redox couple. Nevertheless, in the absence of a theory that would describe such a system we decided to use the existing criteria. Measuring the CVs with the concentrated solution of the electrolyte is in our opinion more relevant considering that a very diluted solution with additional supporting electrolyte does not represent the actual situation in a battery.
[58] Additionally, a small amount of the formed $[Mn^{III}Cl_5]^{2-}$ will react with the platinum of the WE (see Supporting Information), and therefore not be available for a reduction towards $[Mn^{II}Cl_4]^{2-}$, further reducing the i_{pa}/i_{pc}-ratio.
[59] In an actual RFB the same $[Mn^{II}Cl_4]^{2-}$-concentrations would be used in both half-cells to prevent any problems due to osmotic pressure. Unfortunately, in our practical setup we had to use the same amount of electrolyte in each half-cell and therefore decided to use a reduced concentration at the negative electrode. By doing this we mimic the effect that the $[Mn^{II}Cl_4]^{2-}$-concentration decreased during the charge of the battery. Otherwise we would have an excess of $[Mn^{II}Cl_4]^{2-}$ at any time at the negative electrode.
[60] Y. K. Lee, J. Park, W. Lu, *J. Electrochem. Soc.* **2017**, *164*, A2812.
[61] S. Komaba, N. Kumagai, Y. Kataoka, *Electrochim. Acta* **2002**, *47*, 1229.
[62] Y. Maeda, P. Touzain, *Electrochim. Acta* **1988**, *33*, 1493.
[63] pXRD investigations of the affected TF6 material were not conclusive. If dismounted in the potentially charged state, the pXRD signatures were very broad and did at least give no clear evidence for any Mn-intercalation. If the $[BMP]^+$ cation was intercalated, the material is amorphous and not visible in pXRD.
[64] At SoC100 an even higher value of E_{cell} can be expected according to the Nernst equation.
[65] Y. Cheng, X. Wang, S. Huang, W. Samarakoon, S. Xi, Y. Ji, H. Zhang, F. Zhang, Y. Du, Z. Feng, S. Adams, Q. Wang, *ACS Energy Lett.* **2019**, *4*, 3028.
[66] L. Li, S. Kim, W. Wang, M. Vijayakumar, Z. Nie, B. Chen, J. Zhang, G. Xia, J. Hu, G. Graff, J. Liu, Z. Yang, *Adv. Energy Mater.* **2011**, *1*, 394.
[67] J. D. Milshtein, J. L. Barton, T. J. Carney, J. A. Kowalski, R. M. Darling, F. R. Brushett, *J. Electrochem. Soc.* **2017**, *164*, A2487.
[68] R. M. Darling, K. G. Gallagher, J. A. Kowalski, S. Ha, F. R. Brushett, *Energy Environ. Sci.* **2014**, *7*, 3459.
[69] A. P. Abbott, G. Frisch, K. S. Ryder, *Annu. Rev. Mater. Sci.* **2013**, *43*, 335.

© 2021 The Authors. Advanced Energy Materials published by Wiley-VCH GmbH